Imaging of Adeno-Associated Viral Capsids for Purposes of Gene Editing Using CEST NMR/MRI

By

Bonnie Lam

A dissertation submitted in partial satisfaction of the

requirements for the degree of

Joint Doctor of Philosophy
with University of California, San Francisco

in

Bioengineering

in the

Graduate Division

of the

University of California, Berkeley

Committee in charge:

Professor Moriel Vandsburger, Chair
Professor Steven Conolly
Professor Peder Larson
Professor Chunlei Liu

Spring 2024

Abstract

Imaging of Adeno-Associated Viral Capsids for Purposes of Gene Editing
Using CEST NMR/MRI

by

Bonnie Lam

Doctor of Philosophy in Bioengineering

University of California, Berkeley

Professor Moriel Vandsburger, Chair

Gene therapy employing AAV vector-mediated gene delivery has undergone substantial growth in recent years with promising results in both preclinical and clinical studies, as well as emerging regulatory approval. However, the inability to quantify the efficacy of gene therapy from cellular delivery of gene editing technology to specific functional outcomes is an obstacle for efficient development of gene therapy treatments. Building upon prior works that utilized the chemical exchange saturation transfer (CEST) reporter gene lysine-rich protein, we hypothesized that AAV viral capsids may generate endogenous CEST contrast from an abundance of surface lysine residues.

NMR experiments were performed on isolated solutions of AAV serotypes 1-9 on a Bruker 800 MHz vertical scanner. *In vitro* experiments were performed for testing of CEST NMR contrast of AAV2 capsids under varying pH, density, biological transduction stage, and across multiple serotypes and mixed biological media. Reverse transcriptase (RT)-polymerase chain reaction (PCR) was used to quantify virus concentration. Subsequent experiments at 7 T optimized CEST saturation schemes for AAV contrast detection and detected AAV2 particles encapsulated in a biocompatible hydrogel administered in the hind limb of mice.

CEST NMR experiments revealed CEST contrast up to 52% for AAV2 viral capsids between 0.6-0.8 ppm. CEST contrast generated by AAV2 demonstrates high levels of CEST contrast across a variety of chemical environments, concentrations, and saturation schemes. AAV2 CEST contrast displayed significant positive correlations with capsid density (R^2>0.99, P<0.001), pH (R^2=0.97, P=0.01), and viral titer per cell count (R^2=0.92, P<0.001). Transition to a preclinical field strength yielded up to 11.8% CEST contrast following optimization of saturation parameters. *In vivo* detection revealed statistically significant molecular contrast between viral and empty hydrogels using both mean values (4.67±0.75% AAV2 vs. 3.47±0.87% empty hydrogel, p = 0.02) and quantile analysis. AAV2 viral capsids exhibit strong capacity as an endogenous CEST contrast agent and can potentially be used for monitoring and evaluation of AAV vector-mediated gene therapy protocols.

DEDICATION

To everyone who has played a part in guiding and supporting me during this period of my life,
I offer you my sincerest thanks.

TABLE OF CONTENTS

DEDICATION ..... **i**

LIST OF FIGURES ..... **iv**

LIST OF TABLES ..... **v**

CHAPTER ONE: ADENO-ASSOCIATED VIRAL VECTORS FOR GENE THERAPY **1**

Introduction 1

Structure of AAV 1

Serotypes and Variants 1

AAV-Mediated Gene Therapy 2

CHAPTER TWO: CHEMICAL EXCHANGE SATURATION TRANSFER **4**

Overview of Chemical Exchange Saturation Transfer 4

Implementation and Considerations of CEST 5

Applications of CEST 6

CHAPTER THREE: NMR SPECTROSCOPY OF ADENO-ASSOCIATED VIRAL CAPSIDS REVEALS POTENTIAL FOR DETECTION VIA CEST NMR **10**

Introduction 10

Methods 11

Conventional NMR Spectroscopy of AAV2 11

CEST NMR of AAV Capsids in Solution 11

CEST NMR of Cellular Transduction of AAV Capsids 11

CEST Contrast Analysis 11

Results 12

Discussion 13

Acknowledgements 14

CHAPTER FOUR: OPTIMIZATION OF CEST MR IMAGING FOR NONINVASIVE DETECTION OF ADENO-ASSOCIATED VIRAL PARTICLES **21**

Introduction 21

Methods 21

Imaging Protocol 21

CEST Contrast Analysis 21

Results 22

Discussion 23

Acknowledgements 23

CHAPTER FIVE: *IN VIVO* CEST CONTRAST QUANTIFICATION OF AAV PARTICLES FOLLOWING INTRAMUSCULAR HYDROGEL-BASED DELIVERY IN MICE **27**
Introduction 27
Methods 27
Synthesis of PEG Hydrogel 27
MR Imaging of Empty and Viral Hydrogel in Mice at 7T 28
Image Analysis of Hydrogel CEST Data 29
Statistical Analysis 29
Results 29
Discussion 29
Acknowledgements 30
CHAPTER SIX: CONCLUSIONS AND PERSPECTIVES **33**
Summary of Key Findings 33
Limitations and Future Works 33
REFERENCES **34**

LIST OF FIGURES

Figure 2.1. Chemical Exchange Saturation Transfer (CEST) Mechanism..... 8
Figure 2.2. DIACEST Contrast Agents. 9
Figure 3.1. NMR Spectroscopy of AAV2 Viral Capsids..... 15
Figure 3.2. CEST-NMR of AAV2 Viral Capsids..... 16
Figure 3.3. CEST Contrast Across Saturation Powers 17
Figure 3.4. CEST Contrast of AAV2 Across Concentrations, pH, and Saturation Power ... 18
Figure 3.5. CEST Contrast Across AAV Serotypes 19
Figure 3.6. Detection of AAV2 Internalization. 20
Figure 4.1. Representative Z-spectra and Lorentzian Fitting of AAV2 at 7 T 25
Figure 4.2. Z-spectra and Lorentzian Fitting of AAV2 in Presence of Background Signal . 26
Figure 5.1. Box-Whisker Plots of CEST Contrast Values in Empty Hydrogel vs. AAV Hydrogel In Vivo at 7 T 31
Figure 5.2. Representative CEST Contrast Maps of Empty and AAV Hydrogel In Vivo at 7 T 32

LIST OF TABLES

Table 4.1. Optimized CEST-MRI Saturation Parameters 24

CHAPTER ONE:
ADENO-ASSOCIATED VIRAL VECTORS FOR GENE THERAPY

Introduction

Recent advances in gene/genome editing and gene therapy have opened the possibility of a new era of *in vivo* somatic cell gene/genome editing[1]. Increasingly, adeno-associated virus (AAV) vectors have been utilized for gene/genome editing and in gene therapy approaches, and as delivery vehicles for gene/genome editing machinery including CRISPR/Cas9 and novel variants. AAV vectors are particularly attractive delivery vehicles due to generalized non-pathogenicity, organ specificity, replication defectiveness, and low immunogenicity[2].

Structure of AAV

AAV is a helper-dependent parvovirus originally discovered in 1965 as a contaminant in adenovirus preparations[3]. As a dependovirus, replication of AAV is generally supported by the presence of a helper virus such as adenovirus[4]. Consisting of a 4.7 kb single-stranded DNA genome within a nonenveloped icosahedral capsid[5], AAVs have a genome with 3 open reading frames (ORF) flanked by inverted terminal repeats (ITRs) that serve to signal viral replication and packaging[2]. More specifically, the *rep* ORF encodes for 4 nonstructural proteins with roles in viral replication, transcriptional regulation, genomic integration, and virion assembly, whereas the *cap* ORF encodes for 3 structural proteins (VP1-3) that assemble to form a 60-mer viral capsid[6]. VP1 is plays a role in infection, VP2 is responsible for nuclear transfer of capsid proteins, and VP3 is involved in binding of the virus to cell surface receptors and viral particle formation in the host cell[7]. The third ORF is an alternate reading frame that produces the assembly-activating protein, which localizes AAV capsid proteins in the nucleolus and aids in the capsid assembly process[8,9]. Recombinant AAVs (rAAV) for purposes of gene editing have the target gene inserted between the ITRs; the *rep* and *cap* genes are then provided *in trans* along with the helper virus during vector production[9]. Resulting rAAVs are capable of transducing both dividing and nondividing cells, with stable transgene expression that can potentially last for years in postmitotic tissue[2].

Serotypes and Variants

There exist 11 naturally occurring serotypes and over 100 different variants of AAV derived from both human and nonhuman tissues, each with unique differences in amino acid sequence and subsequently, differences in gene delivery properties[2]. For instance, AAV2, which is the most widely used AAV serotype for gene therapy studies[2], utilizes a heparan sulfate proteoglycan (HSPG) attachment receptor[10] and has been used for gene therapy in renal tissues[11,12], hepatocytes[13], retina[14–16], central nervous system (CNS)[17,18], and skeletal muscles[19], whereas AAV9 employs a terminal N-linked galactose attachment receptor[10] and has been investigated for gene editing in cardiac muscle tissue[20–23], photoreceptor cells[24], skeletal muscles[20], and pancreatic cells[20]. Accordingly, differences also exist among the other serotypes of AAV that influence their respective tropism and transduction efficiency for different organs of the body[10,25].

Although naturally occurring AAV variants have been used for gene therapy, wild-type vector variants exhibit several limitations, including reactions to pre-existing neutralizing antibodies (NAbs), low transduction efficiency of certain types of tissue, off-target transduction, and small genetic capacity[26]. As high as 85% of the population demonstrates prior exposure to wild-type AAV particles[27], making it challenging for AAV vectors to reliably circumvent cell-mediated immunity in order to infect host cells in the target tissue. Poor transduction abilities in an AAV vector would lead to increased viral load required for sufficient transduction of the tissue or may even result in a lack of positive gene therapy outcomes. In addition, off-target transduction of the liver or other tissues can lead to reduced therapeutic efficacy following administration of the gene therapy delivery vehicle, toxicity, or triggering of undesired immune responses[28]. The small packaging size of AAVs also poses a problem due to some genes exceeding the gene capacity available for delivery, such as the human dystrophin gene related to Duchenne muscular dystrophy (DMD) with a coding sequence size of approximately 11.5 kb[28].

In response to the obstacles presented by naturally occurring AAV serotypes and the advantages of AAV vectors as suitable carriers for gene therapy studies, development of novel AAV variants with optimized gene delivery properties has been increasingly explored in recent years. Various strategies have been employed for modifying the characteristics of AAV capsids for enhanced tropism, including rational design and directed evolution approaches. Rational design of novel variants involves altering capsid structures by taking into consideration understanding of the capsid and its host interactions, including receptor interactions that affect proper transduction[26]. This approach has led to variants such as AAVrh74, which was discovered by mutagenizing capsids at gene sequence sites corresponding to reduced galactose binding in order to achieve lower levels of off-target transgene transduction and expression in the liver[29].

Directed evolution, however, is implemented via random mutagenesis or recombination for generation of large, diverse protein libraries with novel functions, and subsequent high-throughput rounds of selection for determination of variants with improved functionality[5,30]. Unlike the approach used in rational design, directed evolution does not require extensive prior knowledge of the protein being optimized[31]. Directed evolution has successfully led to the generation of variants such as mutants with an integrin-binding Arg-Gly-Asp (RGD) motif displaying up to 100-fold increased transduction efficiency compared to wild-type AAV2[32] or random peptide insertions that resulted in up to 40-fold increased gene transfer in endothelial cells compared to AAV2[33].

AAV-Mediated Gene Therapy

AAV-mediated gene therapy has been explored across a diverse range of applications over the past few decades, demonstrating promising treatment outcomes in varying types of tissue alongside advancements in development of novel variants, improved understanding of host-receptor attachment interactions, and exploration of different routes of delivery. Most notably, successful AAV gene therapies that have obtained regulatory approval for commercial use include Glybera[34], Luxturna[35], and Zolgensma[36].

Approved in 2012, Glybera, or alipogene tiparvovec, utilizes a non-replicating rAAV1 vector for the treatment of lipoprotein lipase (LPL) deficiency[34]. Lipoprotein lipase deficiency (LPLD) is a rare autosomal recessive disease originating from mutations in the gene encoding for LPL or for other proteins affecting LPL function. Since LPL plays a central role in catabolism of triglyceride-rich lipoproteins, LPLD often results in hyperchylomicronaemia and severe hypertriglyceridaemia[37]. LPLD is associated with an increased risk of clinical complications such

as diabetes mellitus, and in severe cases, can lead to recurrent, severe, and potentially life-threatening acute pancreatitis and possibly even pancreatic cancer[37]. AAV1-LPL^{S447X} uses an AAV1 vector to deliver a gene for a function-enhancing LPL variant associated with lower plasma triglycerides and lower rate of cardiovascular disease[38]. Following a one-time intramuscular administration of AAV1-LPL^{S447X}, patients with LPLD achieved a 40% reduction in fasting plasma triglyceride levels within 3-12 weeks of injection and a five-fold reduction in the 2-year incidence of pancreatitis[38].

Another example of a successful AAV gene therapy product is Luxturna, or voretigene neparvovec, which was the first FDA-approved gene therapy product for a genetic disease[39]. Inherited retinal diseases (IRDs) are a group of rare disorders characterized by varying degrees of vision loss and retinal degeneration. Affecting approximately 1 in every 2,000 individuals worldwide[40], IRDs encompass conditions including retinitis pigmentosa (RP) and Leber congenital amaurosis (LCA) which exhibit symptoms such as sensitivity to light, cataract formation, and ultimately complete blindness[41]. The *RPE65* gene encodes for a 65 kDa protein in the retinal pigment epithelium (RPE) essential for normal functional vision and also associated with certain IRDs[40,41]. By delivering normal copies of *RPE65* into patients with RPE65-IRDs via a modified non-replicating AAV2 vector delivered through a single subretinal injection, dramatic visual enhancements were achieved, including 100- to 45,000-fold increases in light sensitivity[39].

Spinal muscular atrophy (SMA) is a rare genetic condition from a defect in the survival motor neuron 1 (*SMN1*) gene that causes muscle weakness and degeneration[42]. *SMN2*, a less functional *SMN* gene, produces reduced amounts of full-length SMN proteins and has variable copy number[43]. Infants with spinal muscular atrophy type 1 (SMA1), which is the most common form of spinal muscular atrophy, generally experience decline of motor function by 6 months of age and may require permanent ventilation or die by the time they are 2 years old[42]. Zolgensma, or onasemnogene abeparvovec, offers a solution for young patients with SMA by introducing a functional copy of the *SMN* gene to motor neuron cells via a non-replicating AAV9-based vector[36]. Following a single intravenous infusion of onasemnogene abeparvovec, event-free survival and improved motor function in 3–6-month-old patients with SMA1 were observed[44]. A 5-year follow-up of the START trial found all patients in the therapeutic-dose cohort remained alive and without the need for permanent ventilation[45], which is a significant improvement that brings hope for many children to lead longer, more fulfilling lives. Notably, all the gene therapy products presented in this section that met requirements for regulatory approval were based on non-replicating AAV vectors, as the original AAV dosages introduced are capable of generating strong and long-term gene expression sufficient for effective therapeutic effects.

CHAPTER TWO:
CHEMICAL EXCHANGE SATURATION TRANSFER

Overview of Chemical Exchange Saturation Transfer

Chemical exchange saturation transfer, or CEST MRI[46,47], is a novel magnetic resonance (MR) technique that enables imaging of certain compounds at concentrations that would normally be too low to detect with conventional MR imaging. The underlying mechanism for CEST MR imaging (Figure 2.1) is to apply radiofrequency (RF) irradiation to a solute's exchangeable proton pool and for the saturated protons to then exchange with unsaturated protons in the water pool. The exchange of magnetic saturation results in a reduction in the water signal that allows us to indirectly quantify contrast from the original metabolite. Information derived from CEST MRI regarding the chemical environments and concentrations of certain metabolites within the body can be crucial to assessing physiological functions and pathological conditions[48].

In CEST MRI, saturated magnetization is transferred between the bulk water pool and the compound of interest following application of an RF pulse. As a requirement for this process to successfully occur, the solute of interest must have labile protons that can exchange with the protons within water when the RF pulse is applied at the solute's resonant frequency ($\Delta\omega$)[46]. The chemical exchange of saturated solute protons with unsaturated water protons leads to an attenuation in the water signal that is visible at the solute's resonant frequency, thereby indirectly providing information on the solute itself. Although one simple exchange may not be enough to generate sufficient saturation exchange to induce a noticeable net loss in the water signal, a major advantage of CEST is that the effect of numerous saturation exchanges can accumulate to induce a larger signal difference. The resultant reduction in the water signal can then be detected by employing conventional MR imaging sequences following slight modifications in order to yield content information on the solute of interest[46].

Although CEST is similar to magnetic resonance spectroscopy (MRS) in that it provides information on the content of different chemical compounds, CEST demonstrates exceedingly high levels of sensitivity compared to MRS. The size of the bulk water pool is approximately 55 M (110 M if you count the contribution from both hydrogen protons per water molecule), which is much larger compared to the minimal concentration of the solute of interest[49]. Due to the continual exchange and buildup of saturation in water, detection of certain metabolites can be performed with an increased sensitivity of two or more orders of magnitude higher compared to MRS[49]. Under ideal conditions, even as little at 2 mM of exchangeable protons from a suitable compound may lead to a 2% decrease in the water signal[48].

Furthermore, the CEST effect is not only dependent on the concentration of the solute of interest, but also encompasses other factors that may potentially impact the exchange of protons. This includes determinants such as exchange rate, temperature, and pH[49]. Therefore, CEST imaging can also provide valuable information on the chemical environment of the solute that can potentially be used to assess pathological conditions.

Numerous chemical compounds and metabolites have been identified and investigated as potential CEST targets. These CEST agents can generally be classified based on the nature of the solute into categories including diamagnetic CEST (diaCEST) and paramagnetic CEST (paraCEST)[46]. ParaCEST agents generally have resonant frequencies that are further away (more than 7 ppm) from water, are exogenous, and require external administration. DiaCEST agents, on

the other hand, are generally endogenous metabolites that have resonant frequencies closer to water.

Implementation and Considerations of CEST

CEST imaging consists of two primary components: magnetization preparation and data acquisition. The approach used for magnetization preparation affects the image contrast and involves modification of parameters such as saturation power and pulse type, with the pulse type used being classified as either continuous wave or pulsed wave. Continuous wave is more commonly used as it only requires a single long rectangular RF pulse, enabling simple and straightforward optimization. Despite its advantages, however, use of continuous wave saturation may encounter limitations in hardware or specific absorption rate (SAR)[49]. Pulsed wave saturation, however, can potentially overcome those limitations in hardware and SAR by employing a train of short RF pulses. Utilization of pulse wave saturation comes with more parameters to adjust for in order to achieve optimal contrast detection, including pulse shape, pulse duration, number of pulses, and duty cycle[49].

The data acquisition component of CEST largely affects image quality and scan time. The goal for this portion is to attain a high SNR with reduced image distortion while minimizing the total scan time. The acquisition of CEST images over a range of offset frequencies can result in a longer scan time, therefore making the choice of a rapid imaging pulse sequence (e.g. fast gradient echo, single-shot echo planar imaging (EPI), single-shot fast spin echo (FSE), etc.) crucial[48,49]. The total scan time for CEST acquisition can also be shortened by employing techniques to accelerate data acquisition such as parallel imaging and compressed sensing[50,51], which have demonstrated promising results in achieving acceleration factors of 2-4x without compromising CEST image quality and contrast[52,53].

CEST imaging can also vary in the number of offset frequencies acquired for further analysis. The simplest approach to acquisition only requires the acquisition of CEST images at the target resonance frequency, the corresponding conjugate frequency, and a reference image. Calculation of CEST contrast can then be performed via Magnetization Transfer Ratio Asymmetry[49], which can be determined as $MTR_{asym} = [\ S(-\omega) - S(+\omega)\ ] / S_0$. However, this equation carries the underlying assumption that the CEST spectra is symmetric, which has been proven to be false due to slight differences in magnetization transfer (MT) effects[49]. The equation also assumes zero B_0 inhomogeneity, which is often not the case in practice and can be accounted for through B_0 correction techniques such as sampling multiple frequencies around the target and conjugate frequencies and subsequently shifting the CEST spectrum as needed following B_0 mapping or WAter Saturation Shift Referencing (WASSR) acquisition[54]. CEST imaging can also be performed by acquiring a full Z-spectrum across a range of saturation offset frequencies[48]. This approach requires more time due to repeated image acquisitions, but allows for incorporation of more accurate analysis methods such as applying Lorentzian fitting for different proton pools[55] and apparent exchange-dependent relaxation (AREX)[56] for removal of background MT effects and correction of T_1 relaxation.

B_0 and B_1 inhomogeneities are additional considerations that should be kept in mind when using CEST. Spin saturation following excitation via RF pulses depends on frequency-specific irradiation at different proton frequencies, however, the magnetic field across any object or specimen of interest within the scanner is not perfectly homogenous. Small differences in B_0 across the region of interest would induce slight shifts in resonant frequencies across the Z-spectrum[57].

Therefore, B_0 correction performed on a pixelwise basis is critical for accurate evaluation of CEST effects observed. B_1 inhomogeneities, especially *in vivo*, can also be problematic due to insufficient saturation of the target pool(s) being assessed, leading to lower or inconsistent contrast generation[57]. In this case, appropriate correction following B_1 mapping or inclusion of smaller regions of interest may be useful.

Choice of field strength is another factor that can have a major impact on the outcomes of CEST experiments. Use of a higher B_0 field strength can potentially have multiple advantages, including increased signal sensitivity and SNR. Longer T_1 relaxation times at higher fields can lead to larger observed CEST contrasts due to slower recovery from saturation, thereby allowing for greater accumulation of saturation[47]. Furthermore, the greater frequency separation associated with use of higher field strengths facilitates detection of CEST agents with faster exchange rates and improves detection specificity of multiple CEST agents present[49]. However, higher magnetic fields also come with several disadvantages. Aside from an increase in B_0 inhomogeneities, employing high field strengths may lead to certain amplifier performance and hardware limitations that can hinder use of continuous wave saturation[55]. T_2^* effects increase with field strength as well, in addition to susceptibility effects[58], which may be detrimental to image quality. Safety would be an additional concern due to high SAR deposition - more specifically, SAR increases with the square of the field strength[47], which would make it difficult for imaging especially for clinical purposes. Lastly, scanner cost scales up with field strength, with the cost of MRI scanners scaling up with roughly $1 million per Tesla of field strength[59].

Applications of CEST

CEST has a broad range of applications for assessment of *in vivo* metabolite content (Figure 2.2). Magnetization transfer (MT) is the exchange of magnetization between protons from semi-solid macromolecules to protons in the bulk water pool following the application of an off-resonant RF pulse[48]. The semi-solid tissue components have very short T_2 times, which lead to a broad baseline signal that is present in any given tissue and contributes to the asymmetry of the CEST Z-spectrum[55]. The MT signal generated from macromolecules is sensitive to changes in saturation powers used and becomes more visible at higher levels of saturation. MT has predominantly been used for purposes of neurological MR imaging. Previous studies have shown lower MT values in patients with a history of multiple sclerosis (MS)[60,61], leading to additional investigation of the relationship between levels of MT and lesions[62], nerve injuries[63], and gadolinium retention[60] in MS patients. Utilization of MT has also demonstrated promising results in predicting clinical outcomes in glioma patients following radiotherapy[64], and has been used to probe brain tissue changes in individuals with neurodegenerative diseases such as dementia[65], Alzheimer's Disease (AD)[66–68], Huntington Disease (HD)[69–71], and Parkinson's Disease (PD)[72–74]. Furthermore, detection of MT has been enhanced through novel techniques such as background suppression using a stimulated echo acquisition mode (STEAM)[75] pulse sequence for quantification of MT within a single measurement[76].

CEST contrast for relayed nuclear Overhauser enhancement (NOE) arises from aliphatic and olefinic protons in mobile macromolecules[77]. Unlike the short T_2 times and mechanism for generation of MT contrast via through-space intermolecular dipole-dipole interaction with water, NOE has a relatively long T_2 time and involves both exchange-relayed transfer and cross-relaxation[57,78]. In addition, NOE is more frequency-specific compared to the broad signal from MT since it has resonant frequencies upfield of water at -1.6 ppm and -3.5ppm[77]. NOE has been widely

studied in humans in the contexts of brain tumors and infarction caused by ischemia[78–80]. Detection and differentiation of nephropathies in mice has also been explored through CEST studies probing levels of NOE[77,81,82].

Amide Proton Transfer (APT) contrast arises from exchangeable amide protons in mobile tissue proteins and peptides which display a maximum CEST effect around 3.5 ppm from water[57]. APT CEST is the most widely used CEST imaging, especially for clinical research purposes due to its advantage of sensitive detection relative to other diaCEST imaging for *in vivo* use at 3 T[49]. Endogenous concentrations of amide groups are approximately 5-8 mM in most tissues[48] and amide protons have a slow exchange rate of around 30 Hz that changes based on its surrounding chemical environment due to its base-catalyzed characteristic[48]. These qualities pertaining to amide make APT imaging a promising tool for applications such as pH monitoring and tumor identification and differentiation[57]. Amide exchange slows down with decreasing pH, which has enhanced its utility in pH mapping for identifying ischemic regions of brain tissue in those who have experienced cerebrovascular stroke[83–85]. Decreased cerebral flow during strokes eventually results in lowering of intracellular pH, which in turn causes ATP contrast in the ischemic regions to decrease in response[48]. In tumor regions, elevated concentrations of mobile proteins and peptides generate higher levels of APT contrast through increased intracellular exchange[48]. Evaluation of APT content has been explored for identifying tumor boundaries and assessing tumor grade in both preclinical and clinical studies of brain[86–88] and breast tumors[89–91].

Amine CEST contrast generation is from amino acids and peptides that resonate around 1.8-3.0 ppm from water[49]. Amine protons are similar to amide protons in terms of base catalysis, but have comparably faster exchange rates that can potentially generate stronger overall CEST contrast[48]. Different endogenous metabolites can contribute to amine CEST contrast in differing tissues in the body. For instance, levels of glutamate, which serves as an essential neurotransmitter for excitatory transmission in the central nervous system (CNS), provides valuable information for evaluation of neurological disorders[49,92]. Glutamate CEST (gluCEST) has been used to probe glutamate concentrations in the context of different neurodegenerative disorders, including Parkinson's disease[93], Alzheimer's disease[94], and Huntington's disease[95,96]. Another application of CEST imaging of amine protons is creatine CEST (CrCEST); creatine plays a vital role in catalyzing conversion of creatine (Cr) to phosphocreatine (PCr), which is consumed in the rapid generation of ATP during muscle contraction[49]. Therefore, creatine levels in the muscle are a crucial indicator of muscle energy and metabolism. CrCEST has been useful for revealing early-stage cardiomyopathies[97,98] as well as for examining muscle utilization and recovery following plantar flexion exercise[99,100].

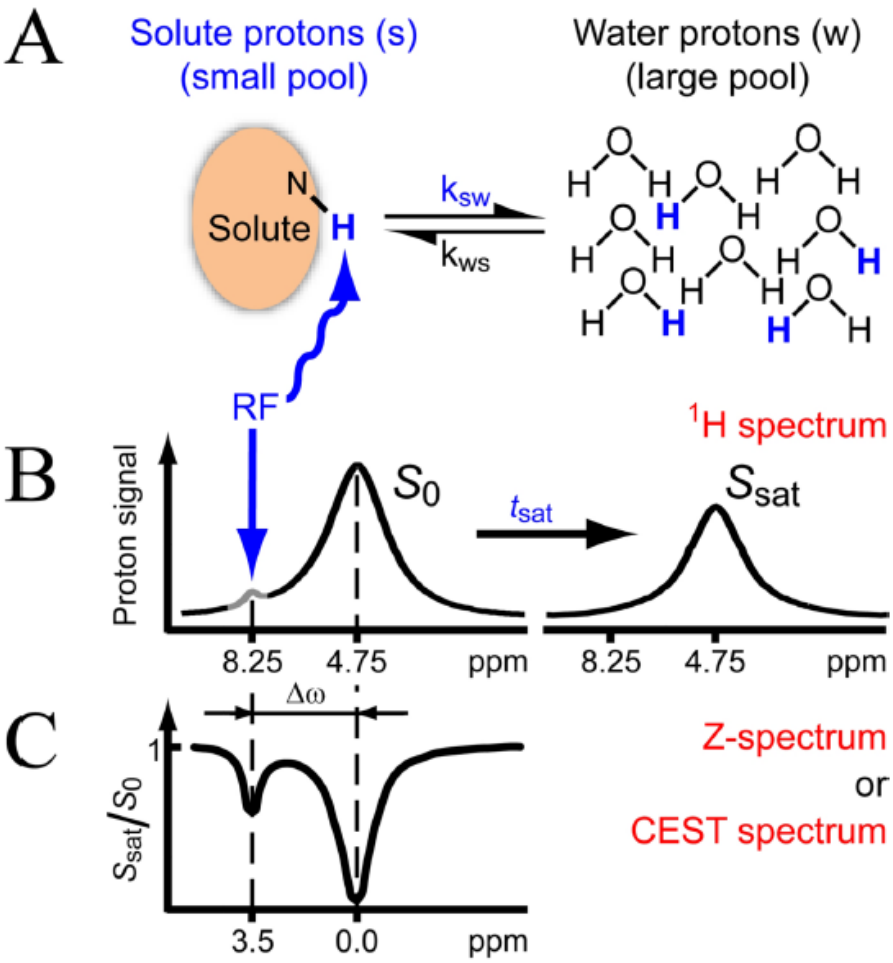

Figure 2.1. Chemical Exchange Saturation Transfer (CEST) Mechanism.[46] (A) Solute protons are subject to RF irradiation at their resonant corresponding resonant frequency. (B) Saturation is then transferred from the solute pool to the bulk water pool following chemical exchange, thereby reducing the water signal. (C) The Z-spectrum displays dips in the signal corresponding to different proton pools.

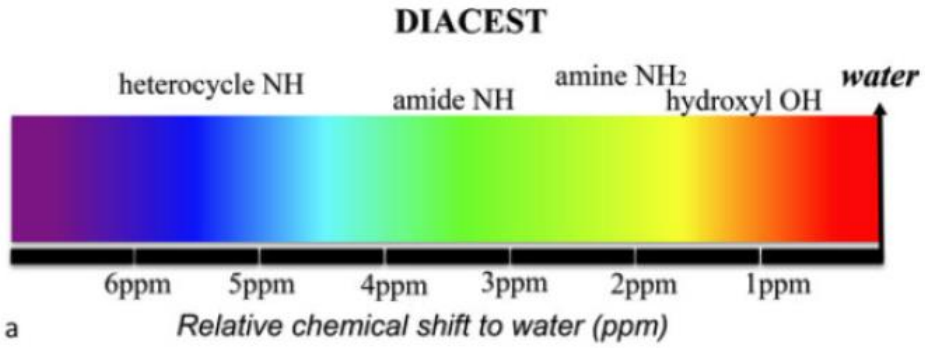

Figure 2.2. DIACEST Contrast Agents.[47] Multicolor spectrum of DIACEST contrast agents with approximate chemical shifts relative to water.

CHAPTER THREE: NMR SPECTROSCOPY OF ADENO-ASSOCIATED VIRAL CAPSIDS REVEALS POTENTIAL FOR DETECTION VIA CEST NMR

Introduction

Clinical and preclinical studies utilizing AAV vectors have explored the efficacy of different serotypes for more targeted delivery in a wide range of disease models across multiple organs, including Duchenne Muscular Dystrophy (DMD)[101–103], hemophilia[104–106], and Alzheimer's Disease (AD)[107,108]. Notably, gene therapy treatments utilizing AAV vectors including Glybera[34], Luxturna[35] and Zolgensma[36] have received approval from US and European regulatory agencies since 2017. In addition, the design of novel engineered AAV variants with enhanced organ tropism and optimized methods for packaging, delivery, and antibody evasion[28,109,110] are evidence of a rapidly evolving field at the cusp of widespread clinical implementation. However, non-invasive assays with which to quantify the efficacy of delivery and editing remain poorly developed and represent a major obstacle to further use.

Conventional clinical assays are appropriate tools for assessment when gene/genome editing or gene therapy succeed in producing a systemic response involving macromolecules that are secreted into the bloodstream. However, when the *in vivo* response to treatment is unclear, the reliance upon invasive biopsies for verification of successful delivery of gene/genome editing cargo remains a boundary condition to the rapid evaluation and evolution of new treatments. Importantly, the dependence upon biopsies increases the likelihood of spatial sampling error, inflicts pain, and may result in complications including sudden death when performed in the heart[111,112]. As the investment in and scope of gene/genome editing and gene therapy continue to expand, there remains an unmet need for the development of a completely non-invasive *in vivo* assay capable of verifying and ideally quantitating the delivery of gene/genome editing cargo.

While targeted molecular MRI approaches have been developed for cell tracking and monitoring transgene expression, no technique exists for tracking AAV particles *in vivo* with MRI. Importantly, surface modification of AAV particles appears to fundamentally alter the transduction efficiency, suggesting that endogenous detection is necessary[113]. Prior studies have demonstrated the ability to track transgene expression of the Lysine Rich Protein[114–117] (LRP), a genetically engineered chemical exchange saturation transfer[46,47,57] (CEST)-MRI reporter peptide. In a previous study from our group, exchange of saturated magnetization at 3.76 ppm between amide protons in Lysine and surrounding bulk water resulted in substantial CEST contrast generated by LRP following AAV9-mediated delivery to the mouse myocardium.

A potential method for monitoring the cellular delivery of AAV capsids containing gene editing machinery is to exploit similarities between AAV capsid surface composition and LRP. Specifically, compared to the 50-lysine polypeptide found in LRP[115], each AAV2 capsid contains over 1,000 lysine residues on its capsid surface[7,113] that we hypothesized may generate sufficient CEST-MRI contrast to enable endogenous detection of AAV particles. In this section, we probed whether AAV2 capsids generate endogenous CEST contrasts through a series of comprehensive multi-field *in vitro* experiments. The parameter space was fully explored under varying pH, capsid density, biological transduction stage in cellular systems, and later across multiple commercially available AAV serotypes.

Methods

Conventional NMR Spectroscopy of AAV2

Conventional NMR experiments were performed on AAV2 (5.23×10^8 viral genomes/μL) in solution using an 800 MHz vertical bore system with a TXI probe (Avance I; Bruker, Ettlingen, Germany). The sample was maintained at pH 7.0 and 37 °C. Additional water-suppressed NMR experiments were conducted under the same conditions. Commercially available AAV2 was purchased from Vector Biolabs and diluted in preparation for NMR experiments.

CEST NMR of AAV Capsids in Solution

To thoroughly test whether AAV capsids generate endogenous CEST contrast a series of experiments were first performed on preparations of AAV2 at varying concentrations and pH. First, CEST NMR experiments were performed on AAV2 (5.26×10^8 viral genomes/μL) in solution (PBS, 0.3% glycerol) and a separate 0.1% poly-L-lysine (PLL) sample as a control at pH 7.0 and 37 °C. Complete Z-spectra were acquired from −5 ppm to +5 ppm with a step size of 0.2 ppm across a range of saturation powers from 3.0 μT to 9.0 μT, serially acquired for all studies. CEST data were extracted as traces at the H_2O resonance from a series of 1D NMR spectra collected at different saturation frequencies. Data were recorded using pulse sequence syszg2df2gppr provided by the manufacturer (Bruker BioSpin Inc., Billerica, MA). The recycle and saturation time were set to 17 sec and 3 sec, respectively. After saturation, the water resonance was excited using a 18° flip angle pulse, that was typically 2.5 μs in duration. The saturation and excitation portions of the sequence were separated by a Z-axis gradient pulse of 1 ms duration and at a field strength of 5 G/cm. Each scan was recorded with a total of 32 K points, using a spectral width of 12820 Hz, and with the carrier frequency set to the water resonance. Data from two scans were signal averaged for each frequency. Next, CEST NMR experiments were performed on AAV2 samples in solution titrated to pH 6 while varying capsid densities between 5.26×10^3 vg/μL and 5.26×10^8 vg/μL. Imaging was performed for AAV2 samples at a concentration of 5.26×10^8 vg/μL while varying pH between 4-7.5 (4, 5, 6, 7.5). CEST NMR experiments were next performed on multiple AAV serotypes (1, 5, 6, 7, 9) at a concentration of 5.26×10^8 vg/μL and pH titrated to a value of 6. All AAV were commercially available (Vector Biolabs).

CEST NMR of Cellular Transduction of AAV Capsids

To test whether AAV2 generates CEST contrast during endosomal transport, HEK293T cells were transduced with AAV2 (MOI 10,000 for 2 million cells) via one hour exposure to viral media at 4°C, after which viral media was removed and replaced with regular media. Cells were harvested at 0-, 30-, 60-, 90-, and 120-minutes following removal of viral media. Control HEK293T cells were exposed to normal media for one hour at 4 °C. Afterwards, endosomes were lysed, isolated, and buffered in solution at pH 6 for CEST NMR experiments. This experiment was performed twice with identical timepoints.

CEST Contrast Analysis

All imaging data were analyzed using custom code written in MATLAB (MathWorks, Natick, MA). For CEST NMR experiments, CEST contrast was calculated as $MTR_{asym}=[S(-\omega) - S(+\omega)]/S_0$.

Results

Conventional (Figure 3.1A) and water-suppressed (Figure 3.1B) NMR spectroscopy performed on solution of AAV2 viral capsids (5.26×10^8 vg/μL) revealed three potential pools of exchangeable protons with adequate concentrations at frequency offsets of 3.6 ppm, 3.0 ppm, and 0.6 ppm (Figure 3.1B). CEST NMR experiments were then conducted to investigate contrast levels at the aforementioned peak frequencies of AAV2 viral capsids. Z-spectra generated by AAV2 (5.26×10^8 vg/μL) reveal broad and significant saturation transfer occurring at upfield frequencies in comparison to a solution of 0.01% PLL as shown in Figure 3.2. Subsequent MTR_{asym} calculations display a strong peak around a frequency offset of 0.6-0.8 ppm. High levels of CEST contrast (~31-52%) were maintained across the range of saturation powers tested (Figure 3.3), with peak contrast increasing with saturation power prior plateauing at higher powers. On average, AAV2 generated CEST contrast of 45.6 ± 5.85% whereas PLL generated CEST contrast of 0.60 ± 0.75%. CEST contrast demonstrated a multi-exponential trend with saturation power; contrast increased rapidly with saturation power up to 6μT, then decreasing thereafter.

The endogenous CEST-MRI contrast generated by AAV2 was explored under different conditions of concentration, pH, and serotype. Mean CEST values for AAV2 samples across saturation powers were 0.81 ± 0.51%, 1.04 ± 0.84%, 3.69 ± 1.48%, and 31.2 ± 4.28% for concentrations of 5.26×10^3 vg/μL, 5.26×10^5 vg/μL, 5.26×10^7 vg/μL, and 5.26×10^8 vg/μL, respectively. The CEST contrast generated by AAV demonstrated a statistically significant pseudo-linear relationship with underlying capsid density ($R^2>0.99$, $P<0.001$). Spectra of CEST contrast as a function of viral capsid density at representative low, medium, and high saturation powers are shown in Figure 3.4A. Mean CEST contrast values for AAV2 (5.26×10^8 vg/μL) across saturation powers were 26.3 ± 10.4%, 31.3 ± 11.2%, 34.5 ± 11.1%, and 45.6 ± 5.9% for pH values of 4, 5, 6, and 7.5, respectively (n = 24 each) as shown in Figure 3.4B. pH and CEST contrast demonstrated a significant correlation; as pH increased, CEST values also increased in most cases ($R^2=0.97$, $P=0.01$).

Evaluation of CEST contrast for different AAV serotypes at a consistent pH of 6.0 revealed preservation of CEST contrast at 0.6 ppm across serotypes (Figure 3.5A) as well as serotype-specific peaks at other offset frequencies (Figure 3.5B,C). Average CEST values across saturation powers were 33.8 ± 5.5%, 33.4 ± 5.7%, 28.7 ± 4.8%, 32.4 ± 5.9%, and 30.7 ± 4.9% for AAV1, AAV5, AAV6, AAV8, and AAV9 respectively. Although contrast was slightly lower than the 34.5 ± 11.1% contrast demonstrated for AAV2, robust CEST contrast was still observed across other serotypes. Interestingly, additional weaker peaks at other offset frequencies were detected for some serotypes in a power-dependent manner.

Detection of stages of AAV2 internalization via changes in CEST contrast displayed differences across timepoints. Quantification of viral titer per cell count in the first run showed a peak value of 0.08 at T=0 minutes prior fluctuations that trended downwards to 0.03 at T=120 minutes (Figure 3.6A). The second run of the same experiment displayed a much different trajectory across time, with viral titer/cell count showing minor fluctuations between 0.008 at T=0 minutes and 0.01 at T=90 minutes preceding a large jump to 0.17 at T=120 minutes (Figure 3.6B). Viral titer/cell count for controls in both runs were near zero ($<10^{-6}$). Corresponding measurements of CEST contrast demonstrated similar trends across timepoints, with contrast fluctuating downwards between 4.52% and 3.66% for the first run (Figure 3.6C) and contrast varying between 3.50% and 2.84% for the first 4 timepoints prior a jump to 6.10% at T=120 minutes (Figure 3.6D).

While direct comparisons of CEST contrast at discrete time points fails to account for the underlying biological stage of transduction, the CEST contrast generated by AAV within endosomes was statistically corelated to viral titer/cell count as quantified by qPCR (R^2=0.92, P<0.001) (Figure 3.6E).

Discussion

In this section we demonstrated that AAV particles, which are commonly used as vehicles for gene/genome editing cargo, generate endogenous contrast on CEST-MRI. Using a series of *in vitro* experiments on isolated viral particles and cellular systems we demonstrated that AAV2 generates concentration dependent CEST contrast at 0.6-0.8 ppm offset from water that correlates with internalized viral content within cells. Importantly, CEST contrast assessed at 0.6 ppm was observed in all AAV serotypes tested.

The endogenous CEST-MRI contrast generated by AAV particles provides a novel mechanism by which to assess the delivery of gene/genome editing machinery to a target tissue. Further development of this methodology could enable noninvasive assessment of an important parameter of vehicle optimization that currently remains outside the scope of noninvasive assays. Presently, the verification of successful gene/genome editing is conventionally performed via biopsy of the target tissue and sequencing for subsequent determination of gene editing efficiency[118,119]. In the absence of a direct method to noninvasively measure the delivery of gene editing cargo to a target tissue, multiple studies have relied upon measurement of a surrogate transgenic reporter peptide. For example, herpes simplex virus type 1-thymidine kinase (HSV1-TK)[120] has been used alongside radioactive positron emission tomography (PET) tracers in oncolytic virotherapy and cancer gene therapy[121–123]. Similarly, the human sodium iodide symporter (hNIS) gene[124,125] has been used to evaluate gene expression patterns in animal models of heart failure and varying types of cancer[126–130]. In other studies, magnetic resonance spectroscopy has been used to assess metabolite changes following gene therapy[131,132]. Similarly MRI allows monitoring of structural changes associated with transgene activity and has been used in previous studies for guiding delivery of an AAV gene therapy dosage as well as tracking subsequent gene expression in Parkinson's disease, Alzheimer's disease, and GM1-gangliosidosis[133–135]. While each of the aforementioned methods are useful to assess transgene efficacy only after successful gene/genome editing, the inclusion of endogenous CEST MRI tracking of AAV particles may enable a coupled assessment of the delivery and subsequent efficacy that is currently not possible.

The structure of the present study was constructed around the hypothesis that AAV2 capsids, each with over 1,000 surface Lysine residues, would generate CEST-MRI contrast similar to a 50-lysine polypeptide (LRP)[115] that has been used as a genetically encoded CEST-MRI reporter protein in oncolytic virotherapy[114], cell tracking[136], and cardiac gene therapy[116]. The exchangeable amide protons within Lysine resonate at 3.76 ppm offset from water. While we observed exchangeable groups at 3.76 ppm, the CEST contrast generated by these protons was significantly less than that observed at 0.6-0.8 ppm. At offsets of 0.6-0.8 ppm the contributors to CEST contrast are predominantly hydroxyl protons. Based on the preservation of this contrast across AAV serotypes and lack of glycosylation of the capsids, the most likely sources of contrast generation are the hydroxyl protons from serine and threonine residues on the AAV capsid surface[137–139].

Acknowledgements

This study was supported by the following funding sources: NIH 1R01HL28592, NIH UH2EB028908, NIH UH3EB028908, AHA 19TPA34850040, DGE 1752814. We also would like to thank Mark Velasquez and A.J. Velasquez-Mao for their insights and contributions towards experiments and analysis results presented in this section.

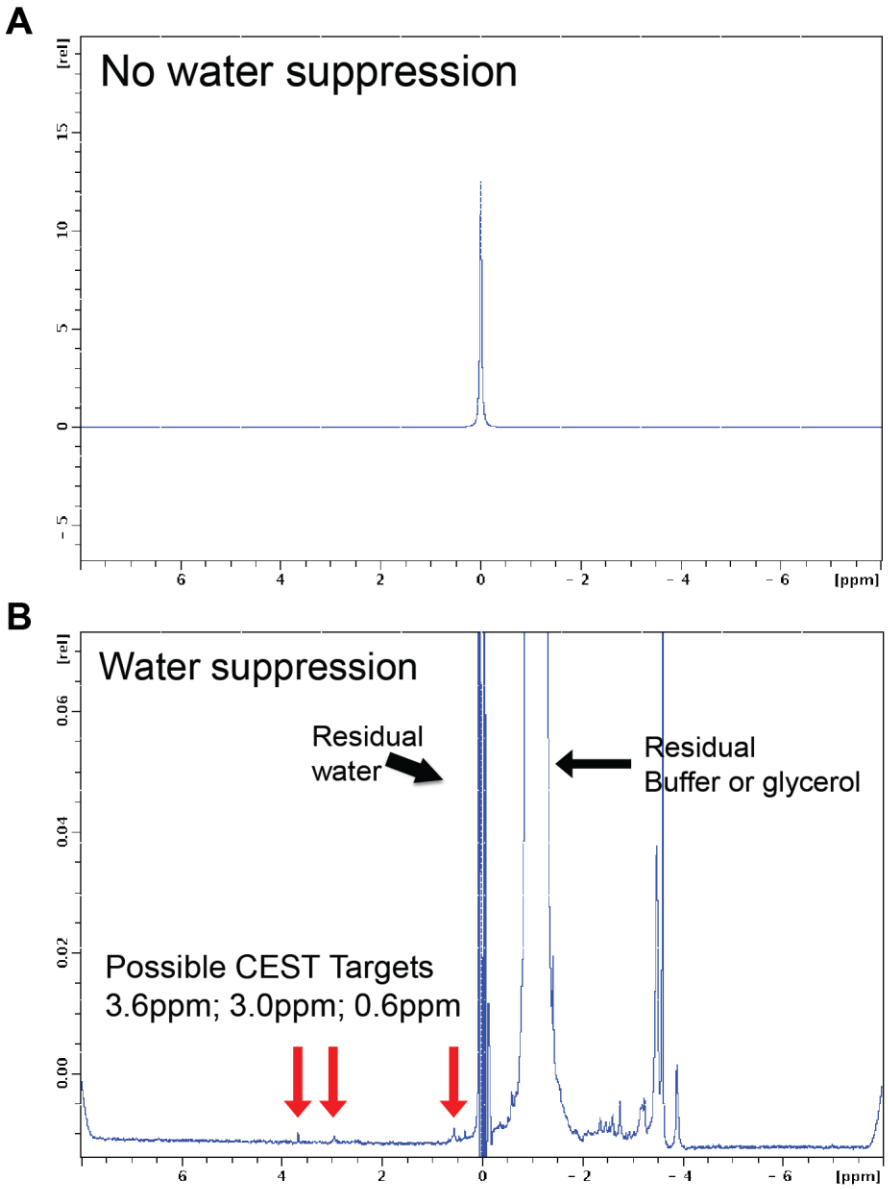

Figure 3.1. NMR Spectroscopy of AAV2 Viral Capsids. (A) Conventional NMR of AAV2 viral capsids. (B) Water-suppressed NMR of AAV2 viral capsids reveal 3 potential CEST targets at 3.6 ppm, 3.0 ppm, and 0.6 ppm.

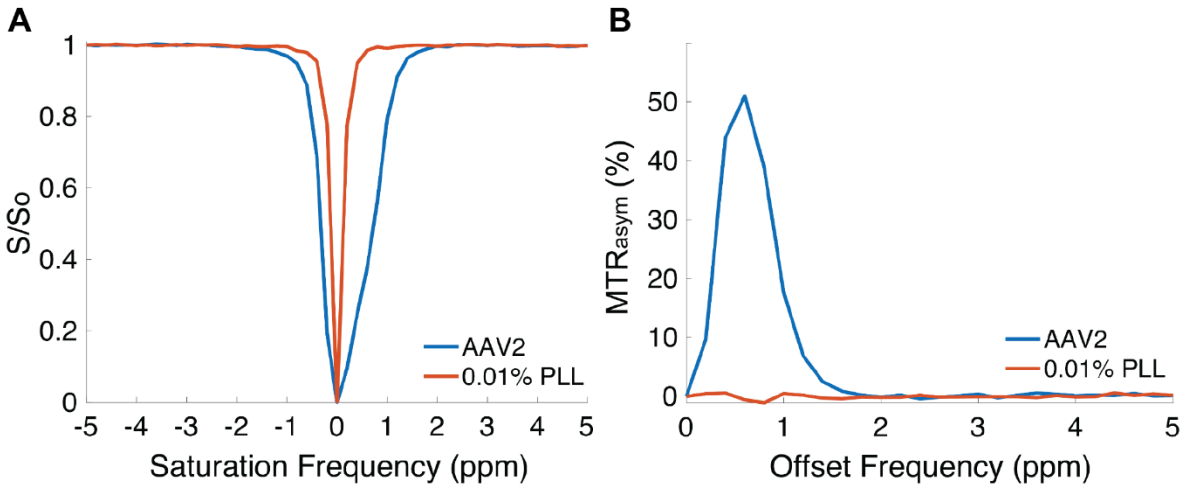

Figure 3.2. CEST-NMR of AAV2 Viral Capsids. (A) Z-spectra of AAV2 (5.26×10^8 vg/μL) and 0.01% poly-L-lysine as a control, acquired at B_1=6.6 μT. (B) Corresponding MTR_{asym} analysis displays high CEST contrast for AAV2 viral capsids around 0.6 ppm.

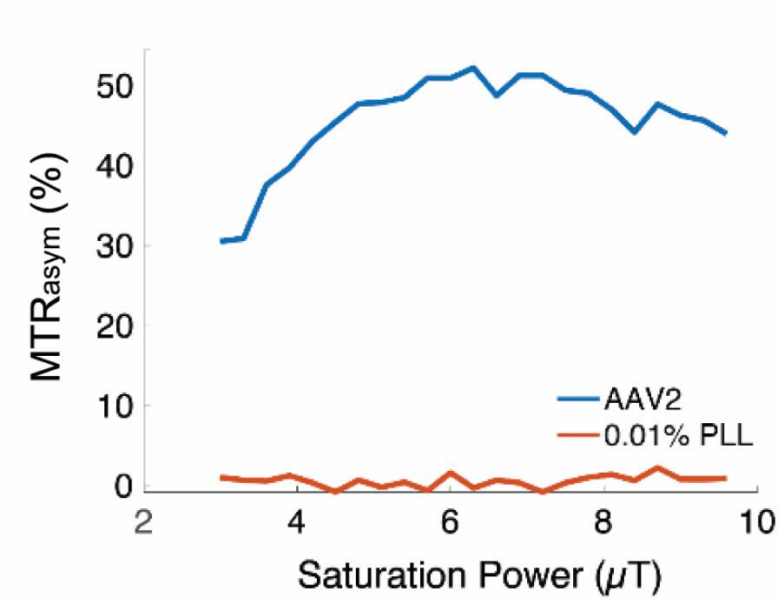

Figure 3.3. CEST Contrast Across Saturation Powers. Resulting CEST contrast of AAV2 (5.26×10^8 vg/μL) and 0.01% PLL as a control across saturation powers ranging from 3 μT to 9.9 μT.

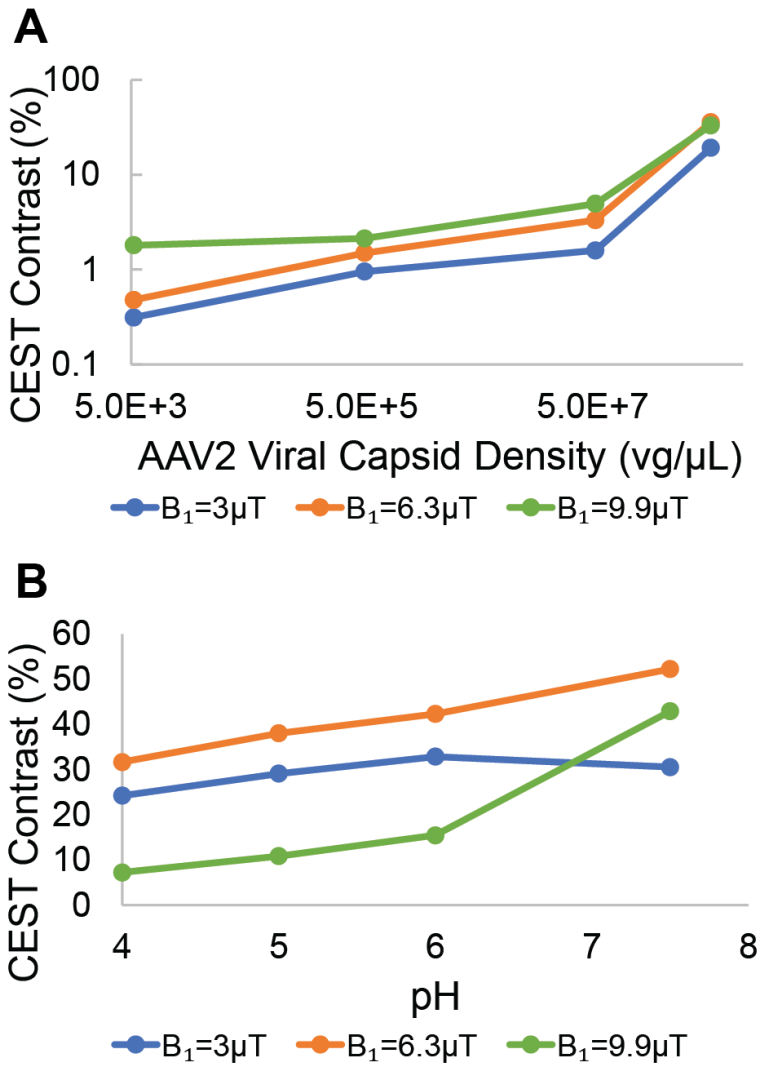

Figure 3.4. CEST Contrast of AAV2 Across Concentrations, pH, and Saturation Power. (A) CEST contrast of AAV2 viral capsids at multiple B_1 powers while varying capsid densities from 5.26×10^3 vg/µL to 5.26×10^8 vg/µL. A significant increase in contrast with increasing capsid density is observed across saturation powers. (B) CEST contrast of AAV2 viral capsids (5.26×10^8 vg/µL) at multiple B_1 powers while varying pH values from 4 to 7.5. A general increase in CEST contrast is observed with increasing pH in most cases.

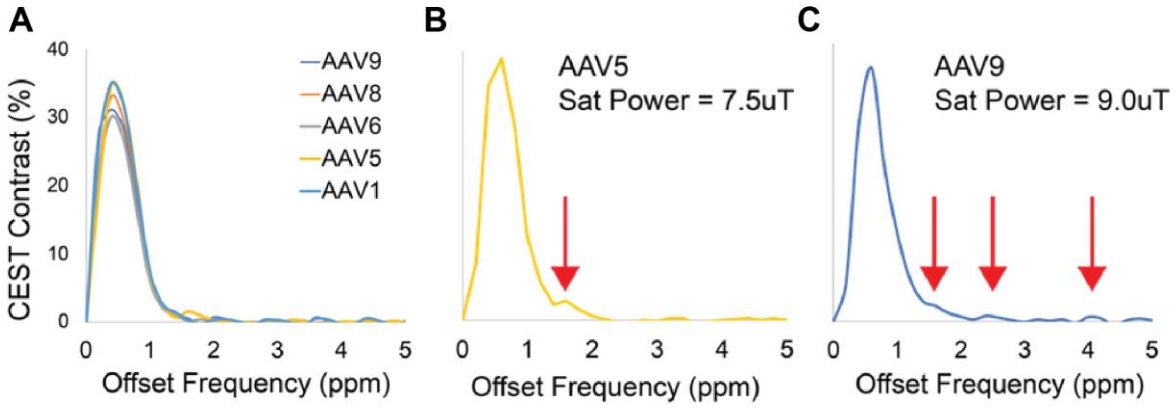

Figure 3.5. CEST Contrast Across AAV Serotypes. Repeated CEST-NMR experiments demonstrated robust CEST contrast around 0.6 ppm across multiple AAV serotypes (A). Additionally, some AAV serotypes exhibited CEST contrast peaks at other offset frequencies (B,C).

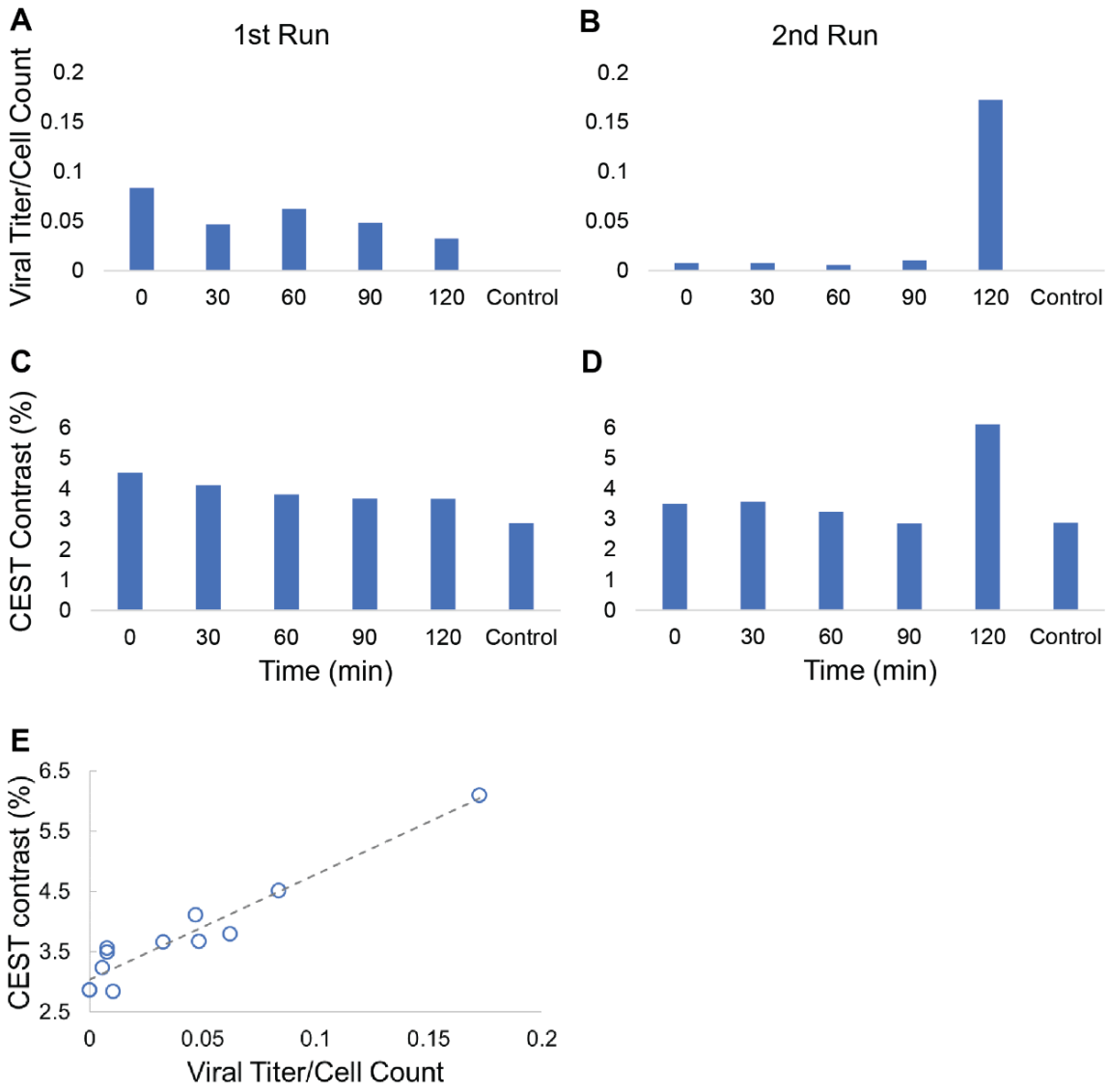

Figure 3.6. Detection of AAV2 Internalization. Repeated CEST-NMR experiments conducted on isolated endosomes harvested from transduced HEK293T cells at multiple timepoints demonstrated varying trends in viral titer per cell count and CEST contrast at 0.8 ppm. (A) Viral titer per cell count in the first run demonstrated fluctuations that gradually decreased over timepoints, whereas (B) viral titer per cell count in the second run displayed a sudden jump at 120 min. (C,D) Resultant CEST contrast in the first and second runs yielded trends that mirrored those shown in viral titer per cell count. (E) Regression analysis of combined data from both runs (including controls) revealed a strong positive correlation for CEST contrast against viral titer/cell count (R^2=0.92, P<0.001).

CHAPTER FOUR:
OPTIMIZATION OF CEST MR IMAGING FOR NONINVASIVE DETECTION OF ADENO-ASSOCIATED VIRAL PARTICLES

Introduction

As mentioned earlier in Chapter Two, changing field strengths for CEST imaging experiments can have several potential impacts on acquired data, including effects on signal sensitivity, SNR, and detection specificity. Based on the findings of exchangeable protons from CEST NMR experiments, we next performed CEST imaging experiments at a field strength of 7 T in order to determine whether endogenous CEST contrast of AAV particles could be detected at pre-clinically relevant field strengths. Additional experiments were performed with AAV capsids in mixed biological media to mimic dilution from biological background signals that would appear *in vivo* and that could potentially affect the quantification of AAV. This includes contributions from other pools that may arise from intracellular proteins, creatine, and other structures would normally be observed in muscle tissue and that may impact the fitting of the AAV pool.

Methods

Imaging Protocol

Phantoms containing AAV2 (5.26×10^8 vg/μL) were imaged at 7 T (PharmaScan; Bruker, Ettlingen, Germany) using a 2×2 array coil (Bruker, Billerica, MA) with dimensions of approximately 60 mm × 105 mm serving as receive-only with volume transmit. Complete Z-spectra acquired from −10 ppm to +10 ppm following varying values for saturation B_1 (1, 1.5, 2, 3, 4 and 5 μT), saturation pulse duration (54.8, 36.5, 27.4, 18.3, 13.7, 11 ms), and saturation duty cycle (60%, 70%, 80%, 85%) across different combinations. A single Gaussian saturation pulse was applied prior acquisition with a centric-ordered GRE readout sequence (TR/TE = 6.44/3.13 ms, matrix = 192 × 192, FOV = 25 mm × 25 mm, slice thickness = 3 mm, number of averages = 2). Reference acquisitions were performed at 150 ppm before and after the acquisition of each Z-spectrum for normalization.

To probe the impact of dilution in background tissue protein content, additional experiments were carried out on a phantom containing cell lysate (6.8 mg protein) and AAV2 (5.26×10^8 vg/μL). Complete Z-spectra were acquired from −10 ppm to +10 ppm following varying values for saturation B_1 (3, 4 and 5 μT), saturation pulse duration (54.8, 36.5, 27.4 ms), and saturation duty cycle (70%, 85%) across all possible combinations. Image properties were identical to those previously stated.

CEST Contrast Analysis

Regions of interest were drawn on reference images prior to calculation of average signal intensities for further analysis. Z-spectra were calculated by normalizing CEST acquisitions to linearly interpolated values of the −10 ppm and +10 ppm acquisitions, followed by temperature correction via linear scaling. In phantoms containing AAV in solution only, CEST contrast was quantified by 2-pool Lorentzian fitting[140] with pools allocated for water and AAV. In phantoms containing AAV and cell lysate in solution, CEST contrast was quantified by 6-pool Lorentzian

fitting with pools allocated for water, magnetization transfer (MT), amine, amide, nuclear Overhauser enhancement (NOE), and AAV. Contributions from different pools to the Z-spectrum were quantified based on a sum of Lorentzian functions as follows:

$$Z(\Delta\omega) = 1 - \sum_{i=1}^{n} L_i \quad [1]$$

With

$$L_i = \frac{A_i\left(\frac{\gamma_i^2}{4}\right)}{\left(\frac{\gamma_i^2}{4}\right)+(\Delta\omega-\omega_i)^2} \quad [2]$$

where A_i, γ_i, and ω_i represent amplitude, FWHM, and resonance frequency relative to water, respectively. Lorentzian peak amplitude values were used as the measure of CEST contrast.

Results

Choices in saturation scheme parameters resulted in large differences in contrast at 7 T as shown in Figure 4.1. Saturation at an offset of 10 ppm represents a region far from water resonance, whereas saturation at an offset of 0 ppm represents a direct saturation of water. Similarly, a saturation offset of 0.8 ppm represents CEST contrast generation by hydroxyl protons on the AAV capsid surface. Images of an AAV2 phantom (5.26×10^8 vg/μL) at multiple frequency offsets display corresponding differences in levels of saturation when the selected saturation scheme generates little to no contrast (Figure 4.1A) or high levels of contrast (Figure 4.1B). Initial attempts to image the AAV2 phantom used varying values of B_1 (1-2 μT), bandwidth (150-250 Hz, corresponding to pulse durations of 11.0-18.3 ms), and duty cycle (60-80%) that resulted in very low CEST contrasts of on average 0.02 ± 0.02%. Representative Z-spectrum and Lorentzian difference plots (Figure 4.1C,E) show minimal contrast generation from AAV2 capsids. Following several saturation scheme adjustments, acquisitions performed while varying B_1 (3-5 μT), bandwidth (50-100 Hz, corresponding to pulse durations of 27.4-54.8 ms), and duty cycle (70-85%) resulted in much higher CEST contrast values that averaged 6.81 ± 4.14%. Analysis of CEST acquisitions revealed multiple saturation schemes that generated contrast levels above 9% in phantoms containing AAV2 (5.26×10^8 vg/μL, Table 4.1). The maximum CEST contrast recorded in phantoms thermostated to an equilibrium temperature of 37 °C was 11.8% (Figure 4.1D,F).

Evaluation of CEST contrast generated by AAV2 in the presence of biological background signals yielded lower, but still detectable levels of contrast as expected. A phantom containing multiple AAV2 samples at different concentrations (5.26×10^3 vg/μL − 5.26×10^8 vg/μL) suspended in cell lysate solution was imaged using the same saturation schemes that generated the highest CEST contrast for virus without biological background (Figure 4.2A). Subsequent analysis of CEST acquisitions yielded mean CEST values of 1.26 ± 1.24%, 1.58 ± 1.27%, 2.01 ± 1.60%, and 3.39 ± 1.93% across saturation schemes for AAV2 capsid concentrations of 5.26×10^3 vg/μL, 5.26×10^5 vg/μL, 5.26×10^7 vg/μL, and 5.26×10^8 vg/μL, respectively. Compared to the CEST NMR results of AAV2 alone, detection of CEST contrast from AAV2 in biological media at 7 T still demonstrated a significant, albeit slightly weaker positive correlation between concentration and CEST contrast (R^2=0.94, P=0.03). At the highest AAV2 concentration tested, optimized

saturation schemes within the conditions tested generated CEST contrast levels of up to 5.85% (Figure 4.2B-F).

Discussion

The reduction in CEST contrast observed in AAV samples prepared in biological media highlights a potential challenge, namely the contributions of other exchanging pools to corresponding Z-spectra. However, the lower CEST contrast values in the presence of background signals are comparable to levels of contrast observed in other studies examining endogenous CEST effects[53,98,141–143]. Importantly, background CEST contrast between 0.5−1.8 ppm will vary between organ systems and is generally low in skeletal muscle, suggesting that minimization of direct saturation of water is a crucial parameter to consider. In specific organs such as the kidney and brain other compounds such as urea (1.0 ppm) and glucose (0.8 ppm), respectively, will likely generate overwhelming background signal obviating potential detection of AAV.

However, identification of optimized CEST parameters for detection of AAV capsids in the presence of biological background signals will be useful for future work probing CEST contrast of AAV particles *in vivo*, particularly for experiments performed at the same preclinical field strength of 7 T.

Acknowledgements

This study was supported by the following funding sources: NIH 1R01HL28592, NIH UH2EB028908, NIH UH3EB028908, AHA 19TPA34850040, DGE 1752814. We also would like to thank Kevin Godines and Wissam AlGhuraibawi for their insights and contributions towards experiments and analysis results presented in this section.

B_1 (μT)	Bandwidth (Hz)	Duty Cycle (%)	Contrast (%)
3	50	70	9.42
3	50	85	9.96
4	75	70	10.44
4	75	85	10.63
4	50	70	11.48
4	50	85	11.35
5	50	70	11.28
5	50	85	11.82

Table 4.1. Optimized CEST-MRI Saturation Parameters. CEST saturation schemes at 7 T tested that exhibit high levels of CEST contrast (>9%) in AAV2 phantom (5.26×10^8 vg/μL).

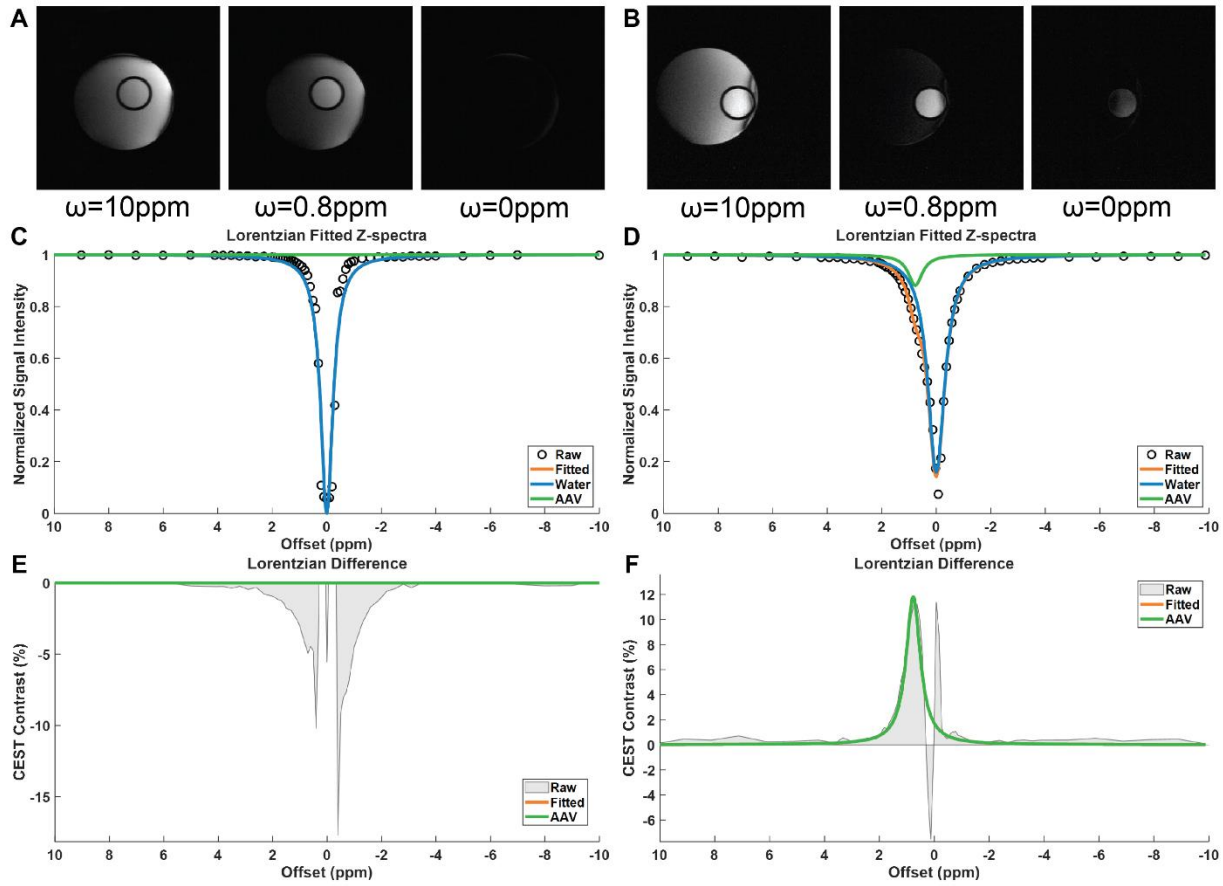

Figure 4.1. Representative Z-spectra and Lorentzian Fitting of AAV2 at 7 T. (A) Images of AAV2 phantom (5.26×10^8 vg/μL) at multiple frequency offsets that correspond to the highest acquired offset (10 ppm) and the resonant frequencies of water (0 ppm) and AAV2 (0.8 ppm). Images were acquired with a saturation scheme of B_1=2 μT, bandwidth=150 Hz, duty cycle=60% that generated minimal CEST contrast. (B) Images of AAV2 phantom (5.26×10^8 vg/μL) at the same frequency offsets but with an optimized saturation scheme of B_1=5 μT, bandwidth=50 Hz, duty cycle=85% that generated high CEST contrast. (C) Representative z-spectrum and 2-pool Lorentzian fitting of AAV2 from the low-contrast saturation scheme. (D) Representative Z-spectrum and 2-pool Lorentzian fitting of AAV2 from the high-contrast saturation scheme with visible peak around 0.8 ppm. (E) Corresponding Lorentzian difference plot showing little to no CEST contrast for AAV2 around 0.8 ppm for low-contrast saturation scheme. (F) Corresponding Lorenzian difference plot displaying 11.85% CEST contrast around 0.8 ppm for high-contrast saturation scheme.

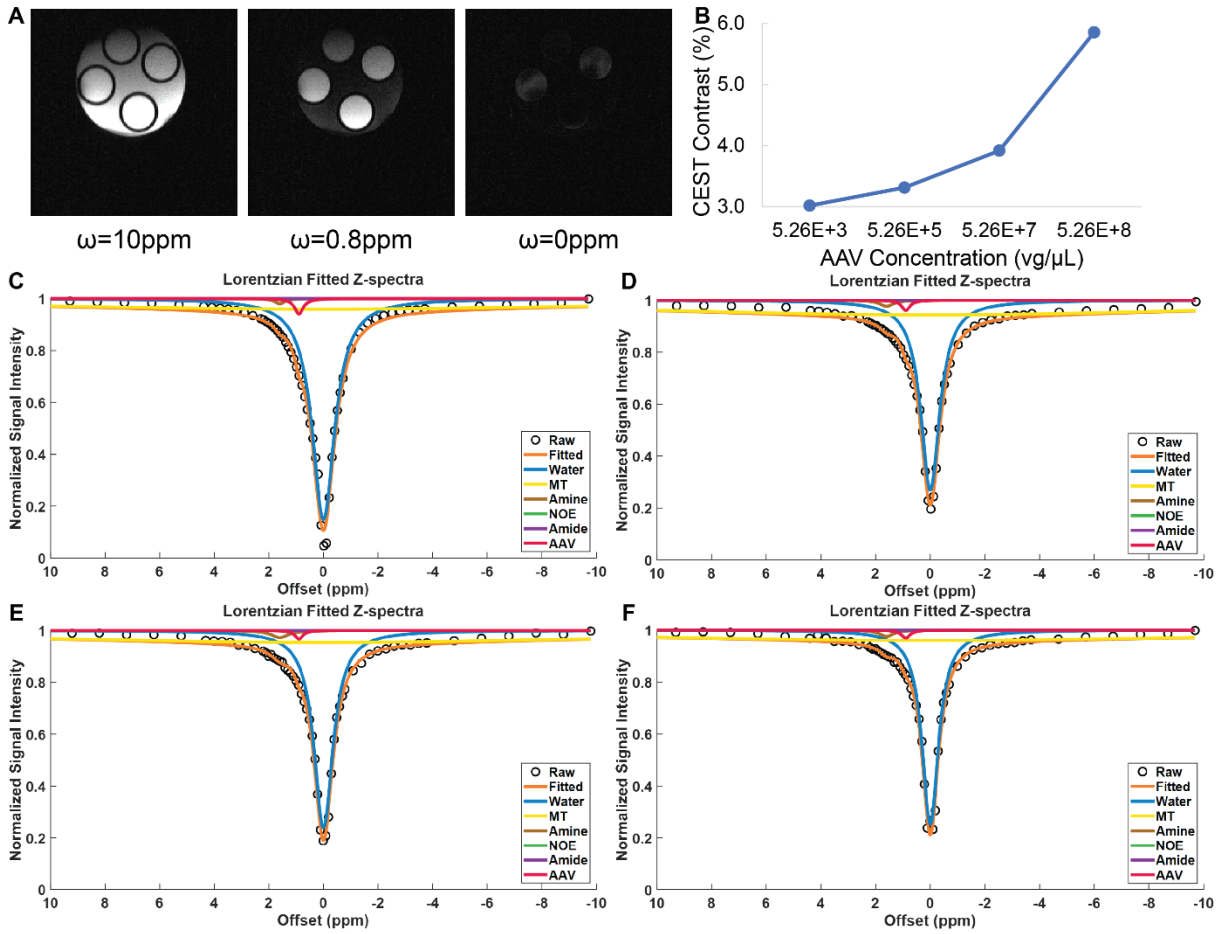

Figure 4.2. Z-spectra and Lorentzian Fitting of AAV2 in Presence of Background Signal. (A) Images of multi-concentration AAV2 phantom and cell lysate phantom at multiple frequency offsets that correspond to the highest acquired offset (10 ppm) and the resonant frequencies of water (0 ppm) and AAV2 (0.8 ppm). Concentrations included in the phantom were 5.26×10^8 vg/μL (top), 5.26×10^7 vg/μL (right), 5.26×10^5 vg/μL (bottom), and 5.26×10^3 vg/μL (left). (B) Resulting contrast across AAV2 concentrations tested using an optimized saturation scheme of B_1=5 μT, bandwidth=50 Hz, duty cycle=70%. Z-spectrum and 6-pool Lorentzian fitting for AAV2 phantom at concentrations of 5.26×10^8 vg/μL (C), 5.26×10^7 vg/μL (D), 5.26×10^5 vg/μL (E), and 5.26×10^3 vg/μL (F).

CHAPTER FIVE:
IN VIVO CEST CONTRAST QUANTIFICATION OF AAV PARTICLES FOLLOWING INTRAMUSCULAR HYDROGEL-BASED DELIVERY IN MICE

Introduction

Hydrogels are hydrophilic crosslinked polymer networks with flexible physical characteristics suitable for facilitation of controlled drug release. Capable of retaining high water content, hydrogels vary in properties such as biodegradability, biocompatibility, stiffness, composition, pH response, and physical response[144]. With varying levels of porosity, hydrogels are capable of steadily releasing encapsulated drugs in response to environmental stimuli and natural degradation over prolonged periods of time ranging from hours to months depending on the formulation[145]. Considerations for designing injectable hydrogels include evaluation of rheological and pre- and post-injection constraints. Injectable therapeutic hydrogels must be compatible with the incorporation of drug, cellular, or other therapeutic cargo being delivered to target tissues, as well as be capable of being administered through a clinical tool such as a needle, catheter, or autoinjector at reasonable applied pressures. Various materials have been used in construction of hydrogels for therapeutic use, including natural sources such as collagen[146], fibrin[147,148], hyaluronic acid[149,150], and alginate[151,152], and synthetic sources such as polyethylene glycol (PEG)[153,154] and polyvinyl alcohol (PVA)[144,155]. The advantages of hydrogels as a controlled, localized delivery mechanism has led to its utilization across multiple applications, including delivery of drugs[145,156], small molecules[157], nucleic acids[158], and proteins[159,160].

Following previous results for optimization of CEST imaging parameters for detection of AAV capsids at 7 T, subsequent *in vivo* experiments using a pre-clinical model of hydrogel-based gene therapy delivery in C57BL/6 mice were conducted to assess CEST-MRI contrast generated by AAV particles. Comparison of viral-loaded hydrogel and control PEG-based hydrogels was performed to evaluate differences in contrast.

Methods

Synthesis of PEG Hydrogel

Unless otherwise noted, materials were obtained from commercial suppliers and used without further purification. AAV2 was purchased from Vector Biolabs. 20 kDa 8-arm PEG-NH_2 with a hexaglycerol core was purchased from JenKem Technology. D-PBS (-), N,N-diisopropylethylamine and D-(+)-glucono-1,5-lactone were purchased from Thermo Fisher Scientific. N,N-Diisopropylcarbodiimide, 1-hydroxybenzotriazole hydrate, 3-carboxy-5-nitrophenylboronic acid and triethylamine were purchased from Sigma-Aldrich. Dichloromethane, dimethyl sulfoxide and methanol were purchased from VWR International. The following abbreviations are used: CH_2Cl_2, dichloromethane; DMSO, dimethyl sulfoxide; MeOH, methanol; Et_2O, diethyl ether.

PEG-BA4 was synthesized according to modified procedures reported in literature[161]. 20 kDa 8-arm PEG-NH_2 with a hexaglycerol core (0.40 g, 0.020 mmol), N,N-diisopropylethylamine (0.087 mL, 0.50 mmol), N,N-diisopropylcarbodiimide (0.039 mL, 0.25 mmol) and 1-

hydroxybenzotriazole hydrate (34 mg, 0.25 mmol) were dissolved in 5.7 mL of a mixture of CH_2Cl_2 and DMSO (2:1, v/v). After 10 min, 3-carboxy-5-nitrophenylboronic acid (63 mg, 0.30 mmol) was added. The mixture was then placed on a rocking platform at 37°C overnight. The resulting yellow transparent gel was dissolved with MeOH (1.0 mL), and the solution was concentrated under reduced pressure. To the residue, MeOH (0.2 mL) was added, and the solution was precipitated with 24 mL of Et_2O and stored at -20°C for 15 min. The supernatant was removed after centrifugation, and the white solid was dissolved in MeOH (4.0 mL). The solution was precipitated with Et_2O (48 mL) and stored at -20°C for 15 min 4 additional times. The white powder was dried in vacuo and dissolved in 30 mL of MilliQ water. The solution was dialyzed against MilliQ water using Slide-A-Lyzer™ G2 Dialysis Cassettes (MWCO: 10K) overnight at r.t. The obtained solution was concentrated with an Amicon® Ultra Centrifugal Filter (MWCO: 10K) and lyophilized to yield PEG-BA4 (0.29 g, 0.014 mmol) as white powder.

PEG-GL was synthesized according to modified procedures reported in the literature[162,163]. To a mixture of 20 kDa 8-arm PEG-NH_2 with a hexaglycerol core (1.0 g, 0.050 mmol), D-(+)-glucono-1,5-lactone (0.86 mg, 4.8 mmol) and MeOH (50 mL), triethylamine (0.17 mL, 1.2 mmol) was added. After stirring at 85 °C overnight, the reaction mixture was concentrated in vacuo. The residue was dissolved in MilliQ water, and purified with Amicon® Ultra centrifugal filter (MWCO: 10K) 4 times. The residue was diluted with 30 mL MilliQ water and dialyzed against MilliQ water using Slide-A-Lyzer™ G2 Dialysis Cassettes (MWCO: 10K) overnight at room temperature. The obtained solution was concentrated with an Amicon® Ultra Centrifugal Filter (MWCO: 10K) and lyophilized to yield PEG-GL (0.76 g, 0.038 mmol) as white powder.

Stock solutions of PEG-BA4 (50 mg/mL) and PEG-GL (60 mg/mL) were prepared in D-PBS (-). For preparation of hydrogels containing viral particles, AAV2 (20 μL solution), 5.0 μL of D-PBS (-) and 125 μL of PEG-GL solution were mixed gently by pipetting. Then, 150 μL of PEG-BA solution was added to the solution and mixed with a pipette tip for approximately 30 seconds to form PEG-gel. The gel without AAV was formulated in a similar manner except using 20 μL of D-PBS (-).

MR Imaging of Empty and Viral Hydrogel in Mice at 7T

Quantification of AAV2 contrast following intramuscular injection was tested via utilization of polyethylene glycol (PEG)-hydrogel-based delivery in mice. 100μL of either empty hydrogel or hydrogel containing approximately 6.67×10^{10} viral particles was administered into mouse skeletal muscle via direct injection into the mouse leg of 10-week-old male C57BL/6 mice from Jackson Laboratory (Bar Harbor, ME). This process was performed for six mice injected with empty hydrogel and seven mice injected with viral hydrogel immediately prior to data acquisition at 7 T (PharmaScan; Bruker, Ettlingen, Germany) using a 2×2 array coil (Bruker, Billerica, MA).

Single-slice axial T2-weighted images (TR/TE = 74.2/2 ms, matrix = 128 × 128, FOV = 25 mm × 25 mm, slice thickness = 1 mm, number of averages = 1) were acquired for identifying the location of the hydrogel. Complete Z-spectra were acquired from −10 ppm to +10 ppm (+/−10, +/−9, +/−8, +/−7, +/−6, +/−5, −4, −3.7, −3.4, −3.1, −2.8, −2.5, −2.2, −1.9, −1.6, −1.3, −1, −0.9, −0.8, −0.7, −0.6, −0.5, −0.4, −0.3, −0.2, −0.1, 0, 0.1, 0.2, 0.3, 0.4, 0.5, 0.6, 0.7, 0.8, 0.9, 1, 1.1, 1.2, 1.3, 1.4, 1.5, 1.6, 1.7, 1.8, 1.9, 2, 2.3, 2.6, 2.9, 3.2, 3.5, 3.8, 4.1 ppm) with a saturation scheme of B_1 = 3 μT, saturation pulse duration of 54.8 ms, and saturation duty cycle of 70%. A single Gaussian saturation pulse was applied prior to acquisition with a centric-ordered GRE readout sequence (TR/TE = 6.44/3.13 ms, matrix = 128 × 128, FOV = 25 mm × 25 mm, slice thickness =

1 mm, number of averages = 1). Reference acquisitions were performed at 150 ppm before and after every 5 frequency offset acquisitions and used for normalization.

Image Analysis of Hydrogel CEST Data

Regions of interest were drawn around the entire mouse leg containing the hydrogel. A pixelwise classifier custom written in MATLAB and employing a combination of correlation coefficient and NMSE thresholds was uniformly applied to all pixels within the region of interest to categorize pixels as belonging to hydrogel, muscle, or noise cases. CEST data from pixels that were classified as hydrogel were then analyzed using 6-pool Lorentzian fitting as previously described to obtain pixelwise CEST contrast maps.

Statistical Analysis

Regression analysis for determining correlation and significance was performed in Excel. Representative values are listed as mean ± standard deviation. Calculation of quantile values and corresponding p-values from bootstrap were performed in R.

Results

A biocompatible polyethyleneglycol based hydrogel was used to implant a reservoir of AAV2 viral particles (6.67×10^{10}) into the hind limb of mice via 100 μL intramuscular injection. The average CEST contrast within hydrogel implants was significantly higher in those containing AAV2 (4.67 ± 0.75% AAV2 vs. 3.47 ± 0.87% empty hydrogel, P=0.02, n=7 AAV2 hydrogel, n=6 empty hydrogel) (Figure 5.1A). Given regional variation in distribution, the comparison of corresponding quantile values revealed a significant difference in CEST contrast values at all tested points in the distributions between empty and viral hydrogels (Figure 5.1B-D). Viral hydrogels exhibited higher CEST contrast values than empty hydrogels at calculated quantile values of 25% (3.66 ± 0.84% vs. 2.38 ± 0.86%, P=0.02), 50% (4.74 ± 0.75% vs. 3.41 ± 0.85%, P=0.01), and 75% (5.73 ± 0.74% vs. 4.55 ± 0.95%, P=0.03). Maps of CEST contrast also displayed regional differences in contrast between empty and AAV hydrogel, as illustrated in a representative example shown in Figure 5.2. These results reveal a mechanism by which to visualize and quantify the distribution of AAV particles within hydrogels following *in vivo* implantation.

Discussion

The use of biocompatible hydrogels as carriers for localized, time-controlled drug release has been widely explored over the last decade[164]. More recently, hydrogel mediated controlled release of AAV vectors has demonstrated enhanced transduction efficiency in poorly perfused tissues, reduced off-target uncontrolled release, and greater delivery duration[165–167]. Conventional MRI can be used to visualize the anatomical distribution of injected hydrogel platforms using T2-weighted imaging, but not the AAV content encapsulated within.

Acquisition of CEST-MRI data enabled noninvasive assessment of AAV encapsulation within a hydrogel following *in vivo* implantation. The CEST contrast measured in the control hydrogel in the current study revealed contributions from hydroxyl protons found on the gluconamide component. While hydrogels containing AAV demonstrated significantly higher CEST contrast values, hydrogel chemistry could be further refined to reduce background contrast

and thereby enhance the detection of AAV particles and quantify the time dependent elution into surrounding tissue. Various injectable hydrogels have been developed in recent years for purposes such as drug delivery and cellular therapy[145], therefore employing a hydrogel without components that may coincide with contrast generated from AAV particles themselves would be useful for more distinct detection.

The viral load for *in vivo* hydrogel administration used in this study was approximately 6.67×10^{10} vg, which is on the lower end of the 10^{9}–10^{12} vg range used in recent studies evaluating AAV-mediated gene therapy treatments for muscular pathologies in mice[168–171]. Based on the results of this study, the lower bound of viral load for sufficient detection via CEST imaging is estimated to be roughly 10^{6} vg per gram of tissue. This approximation assumes some loss in sensitivity in tissue with background signal.

Finally, it is important to note that many of the physiological outcomes of gene therapy and gene/genome editing including tissue fibrosis, metabolic activity, and intracellular protein content can be simultaneously derived from the same CEST-MRI Z-spectrum from which AAV CEST contrast was quantified in the current study, representing a novel method by which to noninvasively track AAV delivery vehicles using entirely endogenous contrast mechanisms. This suggests that with further development CEST-MRI could enable measurement of localized delivery of gene/genome editing cargo alongside cellular outcomes in a single noninvasive assay.

Acknowledgements

This study was supported by the following funding sources: NIH 1R01HL28592, NIH UH2EB028908, NIH UH3EB028908, AHA 19TPA34850040, DGE 1752814. We also would like to thank Tomoko Ogiyama, Fan-Yun Szu, Jingshen Wang, and Phillip B. Messersmith for their insights and contributions towards experiments and analysis results presented in this section.

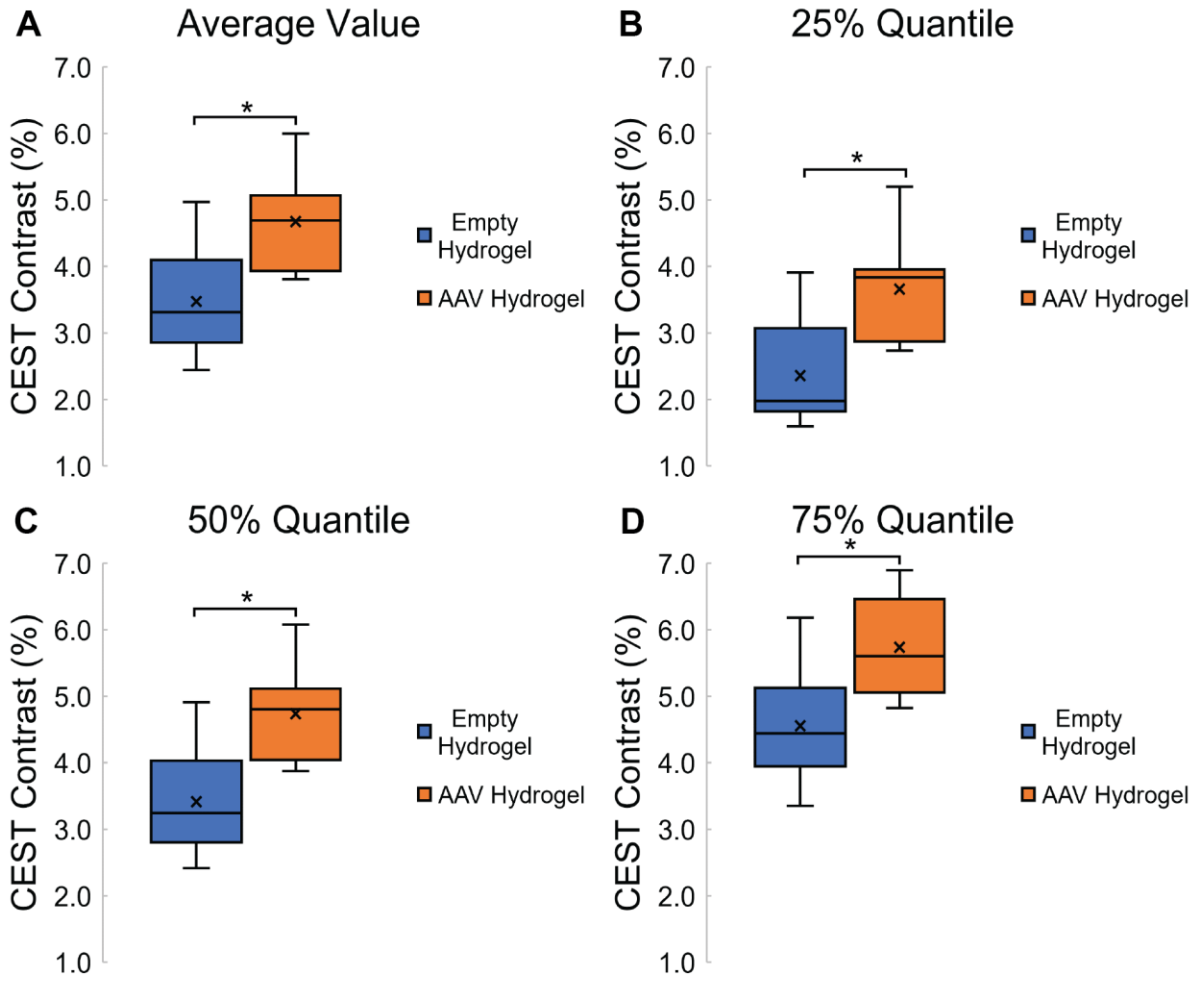

Figure 5.1. Box-Whisker Plots of CEST Contrast Values in Empty Hydrogel vs. AAV Hydrogel In Vivo at 7 T. (A) Box-whisker plots of average CEST contrast values in empty hydrogel and AAV hydrogel in mice skeletal muscle. (B-D) Box-whisker plots of CEST contrast values in empty hydrogel and AAV hydrogel in mice skeletal muscle at quantile values of 25%, 50%, and 75%, respectively.

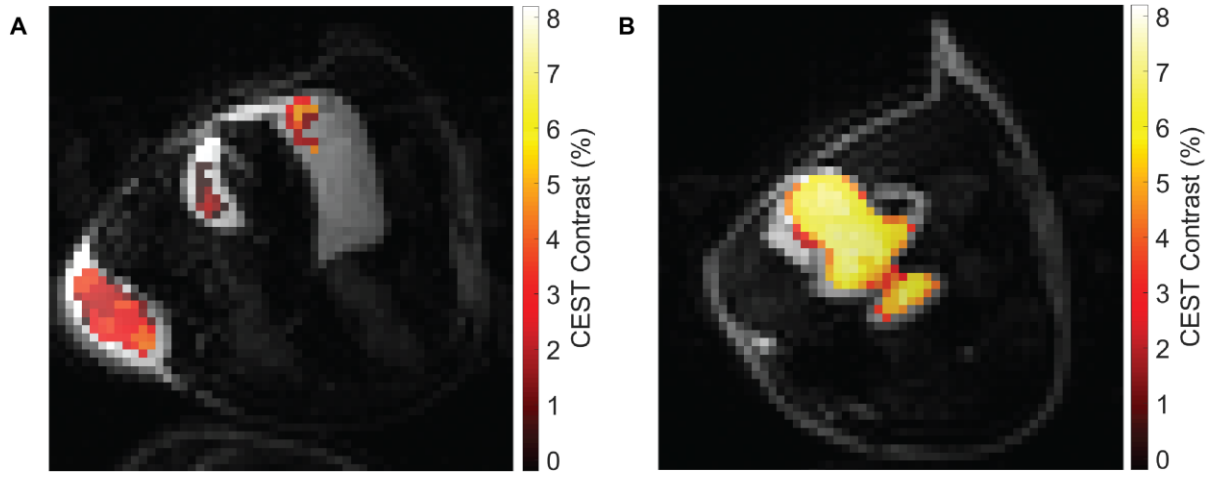

Figure 5.2. Representative CEST Contrast Maps of Empty and AAV Hydrogel In Vivo at 7 T. (A,B) CEST contrast maps overlaid on T2-weighted images for empty hydrogel and AAV-laden hydrogel, respectively.

CHAPTER SIX: CONCLUSIONS AND PERSPECTIVES

Summary of Key Findings

The primary findings of this study are that AAV2 viral capsids generates robust CEST contrast in vitro across a variety of chemical environments, concentrations, and saturation schemes. Significant correlations were observed for AAV2 CEST contrast when adjusting pH, concentration, and viral titer per cell count and should be taken into consideration for further investigation of contrast characteristics. Additional experiments to explore the effectiveness of AAV2 viral capsids as an in vivo endogenous CEST contrast agent for gene therapy tracking is needed.

Limitations and Future Works

Several limitations to this work and potential works to explore need to be discussed. First, we are unable to pinpoint the exact origin of the CEST contrast observed between 0.6-0.8 ppm without creating a library of AAV mutants each selectively missing hydroxyl group containing amino acids on the surface. Based on the consistent contrast observed across AAV serotypes, and the preserved serine and threonine capsid content across serotypes, we suspect that this is the common source of exchangeable protons generating CEST contrast. However, additional studies are required to confirm this assumption.

Second, the experiments in this study were conducted at a high field strength of 7 T. For translation of detecting AAVs at more clinically relevant field strengths using CEST imaging, one challenge is the spectral compression that occurs between 3 T and 7 T. To account for this change, other approaches such as variable-delay multiple-pulse (VDMP)[172] MRI and chemical exchange rotation transfer (CERT)[173] MRI may need to be used.

Third, the non-linear increase in CEST contrast observed between 5.26×10^3 vg/μL and 5.26×10^8 vg/μL suggests that labeling efficiency won't correlate linearly with underlying capsid content. Although quantitative approaches towards CEST imaging have been more recently explored[174,175], CEST contrast correlations with capsid density are semi-quantitative at best – contrast is not generated purely based on concentration but is also affected by additional factors such as pH, as mentioned in Chapter Two. Thus, a direct correlation of CEST contrast to encapsulated viral particle density in future studies may require additional verification in order to create a calibration curve.

Finally, our findings for *in vivo* experiments were conducted immediately following injection of hydrogel containing viral particles, as opposed to at multiple timepoints following administration. Longitudinal tracking and imaging of the viral particles could yield important information for further verification of the potential of CEST contrast of AAV for gene therapy monitoring.

REFERENCES

1. Saha K, Sontheimer EJ, Brooks PJ, et al. The NIH Somatic Cell Genome Editing program. *Nature*. 2021;592(7853):195-204. doi:10.1038/s41586-021-03191-1
2. Kotterman MA, Chalberg TW, Schaffer D V. Viral Vectors for Gene Therapy: Translational and Clinical Outlook. *Annu Rev Biomed Eng*. 2015;17:63-89. doi:10.1146/annurev-bioeng-071813-104938
3. Atchison RW, Casto BC, Hammon WM. Adenovirus-Associated Defective Virus Particles. *Science (80-)*. 1965;149(3685):754-756.
4. Meier AF, Fraefel C, Seyffert M. The Interplay between Adeno-Associated Virus and Its Helper Viruses. *BioDrugs*. 2017;31(1):317-334.
5. Zinn E, Vandenberghe LH. Adeno-associated virus: Fit to serve. *Curr Opin Virol*. 2014;0(1):90-97. doi:10.1016/j.coviro.2014.07.008.Adeno-associated
6. Knipe DM, Howley PM. *Fields' Virology*. 1st ed. Philadelphia, PA: Lippincott Williams & Wilkins; 2007.
7. Xie Q, Bu W, Bhatia S, et al. The atomic structure of adeno-associated virus (AAV-2), a vector for human gene therapy. *Proc Natl Acad Sci U S A*. 2002;99(16):10405-10410. doi:10.1073/pnas.162250899
8. Sonntag F, Köther K, Schmidt K, et al. The Assembly-Activating Protein Promotes Capsid Assembly of Different Adeno-Associated Virus Serotypes. *J Virol*. 2011;85(23):12686-12697. doi:10.1128/jvi.05359-11
9. Flotte TR. Gene therapy progress and prospects: Recombinant adeno-associated virus (rAAV) vectors. *Gene Ther*. 2004;11(10):805-810. doi:10.1038/sj.gt.3302233
10. Issa SS, Shaimardanova AA, Solovyeva V V., Rizvanov AA. Various AAV Serotypes and Their Applications in Gene Therapy: An Overview. *Cells*. 2023;12(5):1-41. doi:10.3390/cells12050785
11. Qi YF, Li QH, Shenoy V, et al. Comparison of the transduction efficiency of tyrosine-mutant adeno-associated virus serotype vectors in kidney. *Clin Exp Pharmacol Physiol*. 2013;40(1):53-55. doi:10.1111/1440-1681.12037
12. Takeda SI, Takahashi M, Mizukami H, et al. Successful gene transfer using adeno-associated virus vectors into the kidney: Comparison among adeno-associated virus serotype 1-5 vectors in vitro and in vivo. *Nephron - Exp Nephrol*. 2004;96(4):119-126. doi:10.1159/000077378
13. Logan GJ, Dane AP, Hallwirth C V., et al. Identification of liver-specific enhancer-promoter activity in the 3′ untranslated region of the wild-type AAV2 genome. *Nat Genet*. 2017;49(8):1267-1273. doi:10.1038/ng.3893
14. Wassmer SJ, Carvalho LS, György B, Vandenberghe LH, Maguire CA. Exosome-associated AAV2 vector mediates robust gene delivery into the murine retina upon intravitreal injection. *Sci Rep*. 2017;7(March):1-10. doi:10.1038/srep45329
15. Yin L, Greenberg K, Hunter JJ, et al. Intravitreal injection of AAV2 transduces macaque inner retina. *Investig Ophthalmol Vis Sci*. 2011;52(5):2775-2783. doi:10.1167/iovs.10-6250
16. Petrs-Silva H, Dinculescu A, Li Q, et al. Novel properties of tyrosine-mutant AAV2 vectors in the mouse retina. *Mol Ther*. 2011;19(2):293-301. doi:10.1038/mt.2010.234
17. Griffey MA, Wozniak D, Wong M, et al. CNS-directed AAV2-mediated gene therapy ameliorates functional deficits in a murine model of infantile neuronal ceroid

lipofuscinosis. *Mol Ther*. 2006;13(3):538-547. doi:10.1016/j.ymthe.2005.11.008
18. Griffey M, Bible E, Vogler C, et al. Adeno-associated virus 2-mediated gene therapy decreases autofluorescent storage material and increases brain mass in a murine model of infantile neuronal ceroid lipofuscinosis. *Neurobiol Dis*. 2004;16(2):360-369. doi:10.1016/j.nbd.2004.03.005
19. Lisowski L, Tay SS, Alexander IE. Adeno-associated virus serotypes for gene therapeutics. *Curr Opin Pharmacol*. 2015;24:59-67. doi:10.1016/j.coph.2015.07.006
20. Inagaki K, Fuess S, Storm TA, et al. Robust systemic transduction with AAV9 vectors in mice: efficient global cardiac gene transfer superior to that of AAV8. *Mol Ther*. 2006;14(1):45-53. doi:10.1016/j.ymthe.2006.03.014
21. Bish LT, Morine K, Sleeper MM, et al. Adeno-associated virus (AAV) serotype 9 provides global cardiac gene transfer superior to AAV1, AAV6, AAV7, and AAV8 in the mouse and rat. *Hum Gene Ther*. 2008;19(12):1359-1368. doi:10.1089/hum.2008.123
22. Pleger ST, Shan C, Ksienzyk J, et al. Cardiac AAV9-S100A1 gene therapy rescues postischemic heart failure in a preclinical large animal model. *Sci Transl Med*. 2011;3(92):92. doi:10.1126/scitranslmed.3002097.Cardiac
23. Pacak CA, Mah CS, Thattaliyath BD, et al. Recombinant adeno-associated virus serotype 9 leads to preferential cardiac transduction in vivo. *Circ Res*. 2006;99(4):3-9. doi:10.1161/01.RES.0000237661.18885.f6
24. Petrs-Silva H, Dinculescu A, Li Q, et al. High-efficiency transduction of the mouse retina by tyrosine-mutant AAV serotype vectors. *Mol Ther*. 2009;17(3):463-471. doi:10.1038/mt.2008.269
25. Zincarelli C, Soltys S, Rengo G, Rabinowitz JE. Analysis of AAV serotypes 1-9 mediated gene expression and tropism in mice after systemic injection. *Mol Ther*. 2008;16(6):1073-1080. doi:10.1038/mt.2008.76
26. Becker J, Fakhiri J, Grimm D. Fantastic AAV Gene Therapy Vectors and How to Find Them— Random Diversification, Rational Design and Machine Learning. *Pathogens*. 2022;11(7). doi:10.3390/pathogens11070756
27. Brockstedt DG, Podsakoff GM, Fong L, Kurtzman G, Mueller-Ruchholtz W, Engleman EG. Induction of immunity to antigens expressed by recombinant adeno- associated virus depends on the route of administration. *Clin Immunol*. 1999;92(1):67-75. doi:10.1006/clim.1999.4724
28. Wang D, Tai PWL, Gao G, Systems P, Tai PWL. *Adeno-Associated Virus Vector as a Platform for Gene Therapy Delivery*. Vol 18.; 2019. doi:10.1038/s41573-019-0012-9.Adeno-associated
29. Chan C, Harris KK, Zolotukhin S, Keeler GD. Rational Design of AAV-rh74, AAV3B, and AAV8 with Limited Liver Targeting. *Viruses*. 2023;15(11). doi:10.3390/v15112168
30. Schaffer D V., Koerber JT, Lim K. Molecular Engineering of Viral Gene Delivery Vehicles. *Annu Rev Biomed Eng*. 2008;10(1):169-194. doi:10.1146/annurev.bioeng.10.061807.160514.Molecular
31. Bartel MA, Weinstein JR, Schaffer D V. Directed evolution of novel adeno-associated viruses for therapeutic gene delivery. *Gene Ther*. 2012;19(6):694-700. doi:10.1038/gt.2012.20
32. Perabo L, Büning H, Kofler DM, et al. In vitro selection of viral vectors with modified tropism: The adeno-associated virus display. *Mol Ther*. 2003;8(1):151-157. doi:10.1016/S1525-0016(03)00123-0

33. Müller OJ, Kaul F, Weitzman MD, et al. Random peptide libraries displayed on adeno-associated virus to select for targeted gene therapy vectors. *Nat Biotechnol*. 2003;21(9):1040-1046. doi:10.1038/nbt856
34. Ferreira V, Twisk J, Kwikkers K, et al. Immune responses to intramuscular administration of alipogene tiparvovec (AAV1-LPLS447X) in a phase II Clinical trial of lipoprotein lipase deficiency gene therapy. *Hum Gene Ther*. 2014;25(3):180-188. doi:10.1089/hum.2013.169
35. Russell S, Bennett J, Wellman JA, et al. Efficacy and safety of voretigene neparvovec (AAV2-hRPE65v2) in patients with RPE65-mediated inherited retinal dystrophy: a randomised, controlled, open-label, phase 3 trial. *Lancet*. 2017;390(10097):849-860. doi:10.1016/S0140-6736(17)31868-8.Efficacy
36. Day JW, Finkel RS, Chiriboga CA, et al. Onasemnogene abeparvovec gene therapy for symptomatic infantile-onset spinal muscular atrophy in patients with two copies of SMN2 (STR1VE): an open-label, single-arm, multicentre, phase 3 trial. *Lancet Neurol*. 2021;20(4):284-293. doi:10.1016/S1474-4422(21)00001-6
37. Scott LJ. Alipogene tiparvovec: A review of its use in adults with familial lipoprotein lipase deficiency. *Drugs*. 2015;75(2):175-182. doi:10.1007/s40265-014-0339-9
38. Gaudet D, Méthot J, Pharm. B, et al. Efficacy and long term safety of alipogene tiparvovec (AAV1-) gene therapy for lipoprotein lipase deficiency: an open LPLS447X label trial. *Gene Ther*. 2013;20(4):361-369. doi:10.1038/gt.2012.43.Efficacy
39. Maguire AM, Bennett J, Aleman EM, Leroy BP, Aleman TS. Clinical Perspective: Treating RPE65-Associated Retinal Dystrophy. *Mol Ther*. 2021;29(2):442-463. doi:10.1016/j.ymthe.2020.11.029
40. Gao J, Hussain RM, Weng CY. Voretigene neparvovec in retinal diseases: A review of the current clinical evidence. *Clin Ophthalmol*. 2020;14:3855-3869. doi:10.2147/OPTH.S231804
41. Kang C, Scott LJ. Voretigene Neparvovec: A Review in RPE65 Mutation-Associated Inherited Retinal Dystrophy. *Mol Diagnosis Ther*. 2020;24(4):487-495. doi:10.1007/s40291-020-00475-6
42. Blair HA. Onasemnogene Abeparvovec: A Review in Spinal Muscular Atrophy. *CNS Drugs*. 2022;36(9):995-1005. doi:10.1007/s40263-022-00941-1
43. Mailman MD, Heinz JW, Papp AC, et al. Molecular analysis of spinal muscular atrophy and modification of the phenotype by SMN2. *Genet Med*. 2002;4(1):20-26. doi:10.1097/00125817-200201000-00004
44. Mendell JR, Al-Zaidy S, Shell R, et al. Single-Dose Gene-Replacement Therapy for Spinal Muscular Atrophy. *N Engl J Med*. 2017;377(18):1713-1722. doi:10.1056/nejmoa1706198
45. Mendell JR, Al-Zaidy SA, Lehman KJ, et al. Five-Year Extension Results of the Phase 1 START Trial of Onasemnogene Abeparvovec in Spinal Muscular Atrophy. *JAMA Neurol*. 2021;78(7):834-841. doi:10.1001/jamaneurol.2021.1272
46. Van Zijl PCM, Yadav NN. Chemical exchange saturation transfer (CEST): What is in a name and what isn't? *Magn Reson Med*. 2011;65(4):927-948. doi:10.1002/mrm.22761
47. Liu G, Song X, Chan KWY, McMahon MT. Nuts and Bolts of CEST MR imaging. *NMR Biomed*. 2013;26(7):810-828. doi:10.1002/nbm.2899
48. Jones KM, Pollard AC, Pagel MD. Clinical applications of chemical exchange saturation transfer (CEST) MRI. *J Magn Reson Imaging*. 2018;47(1):11-27. doi:10.1002/jmri.25838

49. Wu B, Warnock G, Zaiss M, et al. An overview of CEST MRI for non-MR physicists. *EJNMMI Phys*. 2016;3(1). doi:10.1186/s40658-016-0155-2
50. Feng L, Benkert T, Block KT, Sodickson DK, Otazo R, Chandarana H. Compressed Sensing for Body MRI. *J Magn Reson Imaging*. 2017;45(4):966-987.
51. Deshmane A, Gulani V, Griswold MA, Seiberlich N. Parallel MR Imaging. *J Magn Reson Imaging*. 2012;36(1):55-72.
52. Heo H-Y, Zhang Y, Lee D-H, Jiang S, Zhao X, Zhou J. Accelerating Chemical Exchange Saturation Transfer (CEST) MRI by Combining Compressed Sensing and Sensitivity Encoding Techniques. *Magn Reson Med*. 2017;77(2):779-786. doi:10.1002/mrm.26141.Accelerating
53. Lam B, Wendland M, Godines K, Shin SH, Vandsburger M. Accelerated multi-target chemical exchange saturation transfer magnetic resonance imaging of the mouse heart. *Phys Med Biol*. 2021;66(14). doi:10.1088/1361-6560/ac0e78
54. Kim M, Gillen J, Landman BA, Zhou J, Peter CM. WAter Saturation Shift Referencing (WASSR) for chemical exchange saturation transfer experiments. *Magn Reson Med*. 2009;61(6):1441-1450. doi:10.1002/mrm.21873.WAter
55. Van Zijl PCM, Lam WW, Xu J, Knutsson L, Stanisz GJ. Magnetization Transfer Contrast and Chemical Exchange Saturation Transfer MRI. Features and Analysis of the Field-Dependent Saturation Spectrum. *Neuroimage*. 2018;168:222-241. doi:10.1016/j.neuroimage.2017.04.045.Magnetization
56. Zaiss M, Xu J, Goerke S, et al. Inverse Z-spectrum analysis for spillover-, MT-, and T1-corrected steady-state pulsed CEST-MRI - application to pH-weighted MRI of acute stroke. *NMR Biomed*. 2014;27(3):240-252. doi:10.1002/nbm.3054.Inverse
57. Vinogradov, Elena, Sherry, A. Dean, Lenkinski RE. CEST: from basic principles to applications, challenges and opportunities. *J Magn Reson*. 2013;229:155-172. doi:https://doi.org/10.1016/j.jmr.2012.11.024
58. Menon RG, Chang G, Regatte RR. Musculoskeletal MRI applications at ultra-high (7T) field strength. *Magn Reson Imaging Clin North Am*. 2021;29(1):117-127. doi:10.1016/j.mric.2020.09.008.Musculoskeletal
59. Arnold TC, Freeman CW, Litt B, Stein JM. Low-field MRI: Clinical promise and challenges. *J Magn Reson Imaging*. 2023;57(1):25-44. doi:10.1002/jmri.28408
60. Filippi M, Rocca MA, Martino G, Horsfield MA, Comi G. Magnetization transfer changes in the normal appearing white matter precede the appearance of enhancing lesions in patients with multiple sclerosis. *Ann Neurol*. 1998;43(6):809-814. doi:10.1002/ana.410430616
61. Fjær S, Bø L, Lundervold A, et al. Deep gray matter demyelination detected by magnetization transfer ratio in the cuprizone model. *PLoS One*. 2013;8(12). doi:10.1371/journal.pone.0084162
62. Gloor M, Andelova M, Gaetano L, et al. Longitudinal analysis of new multiple sclerosis lesions with magnetization transfer and diffusion tensor imaging. *Eur Radiol*. 2023. doi:10.1007/s00330-023-10173-6
63. Longoni G, Chavez EM, Young K, et al. Magnetization transfer saturation reveals subclinical optic nerve injury in pediatric-onset multiple sclerosis. *Mult Scler J*. 2023;29(2):212-220. doi:10.1177/https
64. Kroh F, von Knebel Doeberitz N, Breitling J, et al. Semi-solid MT and APTw CEST-MRI predict clinical outcome of patients with glioma early after radiotherapy. *Magn Reson*

Med. 2023;90(4):1569-1581. doi:10.1002/mrm.29746
65. Tambasco N, Nigro P, Romoli M, Simoni S, Parnetti L, Calabresi P. Magnetization transfer MRI in dementia disorders, Huntington's disease and parkinsonism. *J Neurol Sci*. 2015;353(1-2):1-8. doi:10.1016/j.jns.2015.03.025
66. Wiest R, Burren Y, Hauf M, et al. Classification of mild cognitive impairment and alzheimer disease using model-based MR and magnetization transfer imaging. *Am J Neuroradiol*. 2013;34(4):740-746. doi:10.3174/ajnr.A3307
67. Carmeli C, Donati A, Antille V, et al. Demyelination in Mild Cognitive Impairment Suggests Progression Path to Alzheimer's Disease. *PLoS One*. 2013;8(8). doi:10.1371/journal.pone.0072759
68. Kiefer C, Brockhaus L, Cattapan-Ludewig K, et al. Multi-parametric classification of Alzheimer's disease and mild cognitive impairment: The impact of quantitative magnetization transfer MR imaging. *Neuroimage*. 2009;48(4):657-667. doi:10.1016/j.neuroimage.2009.07.005
69. Van Den Bogaard SJA, Dumas EM, Hart EP, et al. Magnetization transfer imaging in premanifest and manifest Huntington disease: A 2-year follow-up. *Am J Neuroradiol*. 2013;34(2):317-322. doi:10.3174/ajnr.A3303
70. Van Den Bogaard SJA, Dumas EM, Milles J, et al. Magnetization transfer imaging in premanifest and manifest Huntington disease. *Am J Neuroradiol*. 2012;33(5):884-889. doi:10.3174/ajnr.A2868
71. Ginestroni A, Battaglini M, Diciotti S, et al. Magnetization transfer MR imaging demonstrates degeneration of the subcortical and cortical gray matter in Huntington disease. *Am J Neuroradiol*. 2010;31(10):1807-1812. doi:10.3174/ajnr.A2225
72. Tambasco N, Pelliccioli GP, Chiarini P, et al. Magnetization transfer changes of grey and white matter in Parkinson's disease. *Neuroradiology*. 2003;45(4):224-230. doi:10.1007/s00234-002-0925-5
73. Tambasco N, Belcastro V, Sarchielli P, et al. A magnetization transfer study of mild and advanced Parkinson's disease. *Eur J Neurol*. 2011;18(3):471-477. doi:10.1111/j.1468-1331.2010.03184.x
74. Eckert T, Sailer M, Kaufmann J, et al. Differentiation of idiopathic Parkinson's disease, multiple system atrophy, progressive supranuclear palsy, and healthy controls using magnetization transfer imaging. *Neuroimage*. 2004;21(1):229-235. doi:10.1016/j.neuroimage.2003.08.028
75. Haase A, Frahm J, Matthaei D, et al. MR imaging using stimulated echoes (STEAM). *Radiology*. 1986;160(3):787-790.
76. van Gelderen P, Duyn JH. Background suppressed magnetization transfer MRI. *Magn Reson Med*. 2020;83(3):883-891. doi:10.1002/mrm.27978
77. Shin SH, Wendland MF, Wang J, Velasquez M, Vandsburger MH. Noninvasively differentiating acute and chronic nephropathies via multiparametric urea-CEST, nuclear Overhauser enhancement-CEST, and quantitative magnetization transfer MRI. *Magn Reson Med*. 2023;89(2):774-786. doi:10.1002/mrm.29477
78. Heo H-Y, Jones CK, Hua J, et al. Whole-Brain Amide Proton Transfer (APT) and Nuclear Overhauser enhancement (NOE) Imaging in Glioma Patients Using Low-Power Steady-State Pulsed CEST Imaging at 7T. *J Magn Reson Imaging*. 2016;44(1):41-50. doi:10.1002/jmri.25108.Whole-Brain
79. Jones CK, Huang A, Xu J, et al. Nuclear Overhauser Enhancement (NOE) Imaging in the

Human Brain at 7 T. *Neuroimage*. 2013;77:114-124. doi:10.1016/j.neuroimage.2013.03.047.Nuclear
80. Zaiss M, Windschuh J, Paech D, et al. Relaxation-compensated CEST-MRI of the human brain at 7T: Unbiased insight into NOE and amide signal changes in human glioblastoma. *Neuroimage*. 2015;112:180-188. doi:10.1016/j.neuroimage.2015.02.040
81. Liu J, Han Z, Chen G, et al. CEST MRI of sepsis-induced acute kidney injury. *NMR Biomed*. 2018;31(8):1-11. doi:10.1002/nbm.3942
82. Wang F, Kopylov D, Zu Z, et al. Mapping Murine Diabetic Kidney Disease Using Chemical Exchange Saturation Transfer MRI. *Magn Reson Med*. 2016;76(5):1531-1541. doi:10.1002/mrm.26045.Mapping
83. Sun PZ. Demonstration of magnetization transfer and relaxation normalized pH-specific pulse-amide proton transfer imaging in an animal model of acute stroke. *Magn Reson Med*. 2020;84(3):1526-1533. doi:10.1002/mrm.28223
84. Sun PZ, Wang E, Cheung JS. Imaging acute ischemic tissue acidosis with pH-sensitive endogenous amide proton transfer (APT) MRI - Correction of tissue relaxation and concomitant RF irradiation effects toward mapping quantitative cerebral tissue pH. *Neuroimage*. 2012;60(1):1-6. doi:10.1016/j.neuroimage.2011.11.091.Imaging
85. Wang E, Wu Y, Cheung JS, et al. Mapping tissue pH in an experimental model of acute stroke - Determination of graded regional tissue pH changes with non-invasive quantitative amide proton transfer MRI. *Neuroimage*. 2019;191:610-617. doi:10.1016/j.neuroimage.2019.02.022.Mapping
86. Zhou J, Zaiss M, Knutsson L, et al. Review and consensus recommendations on clinical APT-weighted imaging approaches at 3T: Application to brain tumors. *Magn Reson Med*. 2022;88(2):546-574. doi:10.1002/mrm.29241
87. Zhou J, Heo H-Y, Knutsson L, Van Zijl PCM, Jiang S. APT-Weighted MRI; Techniques, Current Neuro Applications, and Challenging Issues. *J Magn Reson Imaging*. 2019;50(2):347-364. doi:10.1002/jmri.26645.APT-Weighted
88. Goerke S, Breitling J, Korzowski A, et al. Clinical routine acquisition protocol for 3D relaxation-compensated APT and rNOE CEST-MRI of the human brain at 3T. *Magn Reson Med*. 2021;86(1):393-404.
89. Vinogradov E, Keupp J, Dimitrov IE, Seiler S, Pedrosa I. CEST-MRI for body oncologic imaging: are we there yet? *NMR Biomed*. 2023;36(6):1-23. doi:10.1002/nbm.4906
90. Zimmermann F, Korzowski A, Breitling J, et al. A novel normalization for amide proton transfer CEST MRI to correct for fat signal–induced artifacts: application to human breast cancer imaging. *Magn Reson Med*. 2020;83(3):920-934. doi:10.1002/mrm.27983
91. Loi L, Zimmermann F, Goerke S, et al. Relaxation-compensated CEST (chemical exchange saturation transfer) imaging in breast cancer diagnostics at 7T. *Eur J Radiol*. 2020;129(May):109068. doi:10.1016/j.ejrad.2020.109068
92. Cember ATJ, Nanga RPR, Reddy R. Glutamate-weighted CEST (gluCEST) imaging for mapping neurometabolism: An update on the state of the art and emerging findings from in vivo applications. *NMR Biomed*. 2023;36(6):1-21. doi:10.1002/nbm.4780
93. Bagga P, Pickup S, Crescenzi R, et al. In vivo GluCEST MRI: Reproducibility, background contribution and source of glutamate changes in the MPTP model of Parkinson's disease. *Sci Rep*. 2018;8(1):1-9. doi:10.1038/s41598-018-21035-3
94. Haris M, Nath K, Cai K, et al. Imaging of Glutamate Neurotransmitter Alterations in Alzheimer's Disease. *NMR Biomed*. 2013;26(4):386-391. doi:10.1002/nbm.2875.Imaging

95. Pépin J, de Longprez L, Trovero F, Brouillet E, Valette J, Flament J. Complementarity of gluCEST and 1H-MRS for the study of mouse models of Huntington's disease. *NMR Biomed*. 2020;33(7):1-10. doi:10.1002/nbm.4301
96. Pépin J, Francelle L, Carrillo-de Sauvage MA, et al. In vivo imaging of brain glutamate defects in a knock-in mouse model of Huntington's disease. *Neuroimage*. 2016;139:53-64. doi:10.1016/j.neuroimage.2016.06.023
97. Fan ZY, Lin YW, Shi RY, et al. Creatine chemical exchange saturation transfer (CEST) CMR imaging reveals myocardial early involvement in idiopathic inflammatory myopathy at 3T: feasibility and initial experience. *Eur Radiol*. 2023;33(6):3897-3907. doi:10.1007/s00330-022-09363-5
98. AlGhuraibawi W, Stromp T, Holtkamp R, et al. CEST MRI reveals a correlation between visceral fat mass and reduced myocardial creatine in obese individuals despite preserved ventricular structure and function. *NMR Biomed*. 2019;32(7):e4104. doi:10.1002/nbm.4104.
99. Kumar D, Nanga RPR, Thakuri D, et al. Recovery kinetics of creatine in mild plantar flexion exercise using 3D creatine CEST imaging at 7 Tesla. *Magn Reson Med*. 2021;85(2):802-817. doi:10.1002/mrm.28463
100. Kogan F, Harris M, DeBrosse C, et al. In vivo CEST imaging of Creatine (CrCEST) in Skeletal Muscle at 3T. *J Magn Reson Imaging*. 2014;40(3):596-602. doi:10.1002/jmri.24412.In
101. Crudele JM, Chamberlain JS. AAV-based gene therapies for the muscular dystrophies. *Hum Mol Genet*. 2019;28(R1):R102-R107. doi:10.1093/hmg/ddz128
102. Duan D. Systemic AAV Micro-dystrophin Gene Therapy for Duchenne Muscular Dystrophy. *Mol Ther*. 2018;26(10):2337-2356. doi:10.1016/j.ymthe.2018.07.011
103. Chamberlain JR, Chamberlain JS. Progress toward Gene Therapy for Duchenne Muscular Dystrophy. *Mol Ther*. 2017;25(5):1125-1131. doi:10.1016/j.ymthe.2017.02.019
104. Nguyen GN, Everett JK, Kafle S, et al. A long-term study of AAV gene therapy in hemophilia A dogs identifies clonal expansions of transduced liver cells. *Nature*. 2021;39(1):47-55. doi:10.1038/s41587-020-0741-7.
105. Pipe SW. Gene therapy for hemophilia. *Pediatr Blood Cancer*. 2018;65(2):1-8. doi:10.1002/pbc.26865
106. Nienhuis AW, Nathwani AC, Davidoff AM. Gene Therapy for Hemophilia. *Mol Ther*. 2017;25(5):1163-1167. doi:10.1016/j.ymthe.2017.03.033
107. Rosenberg JB, Kaplitt MG, De BP, et al. AAVrh.10-Mediated APOE2 Central Nervous System Gene Therapy for APOE4-Associated Alzheimer's Disease. *Hum Gene Ther Clin Dev*. 2018;29(1):24-47. doi:10.1089/humc.2017.231
108. Griciuc A, Federico AN, Natasan J, et al. Gene therapy for Alzheimer's disease targeting CD33 reduces amyloid beta accumulation and neuroinflammation. *Hum Mol Genet*. 2020;29(17):2920-2935. doi:10.1093/hmg/ddaa179
109. Li C, Samulski RJ. Engineering adeno-associated virus vectors for gene therapy. *Nat Rev Genet*. 2020;21(4):255-272. doi:10.1038/s41576-019-0205-4
110. Naso MF, Tomkowicz B, Perry WL, Strohl WR. Adeno-Associated Virus (AAV) as a Vector for Gene Therapy. *BioDrugs*. 2017;31(4):317-334. doi:10.1007/s40259-017-0234-5
111. Poggio ED, Mcclelland L, Kristina N, et al. Systematic Review and Meta-Analysis of Native Kidney Biopsy Complications. *Clin J Am Soc Nephrol*. 2020;15(11):1595-1602.

doi:10.2215/CJN.04710420
112. Olymbios M, Kwiecinski J, Berman DS, Kobashigawa JA. Imaging in Heart Transplant Patients. *JACC Cardiovasc Imaging*. 2018;11(10):1514-1530. doi:10.1016/j.jcmg.2018.06.019
113. Lee GK, Maheshri N, Kaspar B, Schaffer D V. PEG conjugation moderately protects adeno-associated viral vectors against antibody neutralization. *Biotechnol Bioeng*. 2005;92(1):24-34. doi:10.1002/bit.20562
114. Farrar CT, Buhrman JS, Liu G, et al. Establishing the Lysine-rich Protein CEST Reporter Gene as a CEST MR Imaging Detector for Oncolytic Virotherapy. *Radiology*. 2015;275(3).
115. Gilad AA, McMahon MT, Walczak P, et al. Artificial reporter gene providing MRI contrast based on proton exchange. *Nat Biotechnol*. 2007;25(2):217-219. doi:10.1038/nbt1277
116. Meier S, Gilad AA, Brandon JA, et al. Non-invasive detection of adeno-associated viral gene transfer using a genetically encoded CEST-MRI reporter gene in the murine heart. *Sci Rep*. 2018;8(1):1-10. doi:10.1038/s41598-018-22993-4
117. Perlman O, Ito H, Gilad AA, et al. Redesigned reporter gene for improved proton exchange-based molecular MRI contrast. *Sci Rep*. 2020;10(1):1-9. doi:10.1038/s41598-020-77576-z
118. Shendure J, Balasubramanian S, Church GM, et al. DNA sequencing at 40: Past, present and future. *Nature*. 2017;550(7676). doi:10.1038/nature24286
119. Slatko BE, Gardner AF, Ausubel FM. Overview of next generation sequencing technologies (and bioinformatics) in cancer. *Mol Biol*. 2018;122(1):1-15. doi:10.1002/cpmb.59.Overview
120. McCracken MN. Thymidine Kinase PET Reporter Gene Imaging of Cancer Cells In Vivo. In: Dubey P, ed. *Reporter Gene Imaging: Methods and Protocols*. New York, NY: Springer New York; 2018:137-151. doi:10.1007/978-1-4939-7860-1_11
121. Concilio SC, Russell SJ, Peng KW. A brief review of reporter gene imaging in oncolytic virotherapy and gene therapy. *Mol Ther - Oncolytics*. 2021;21(June):98-109. doi:10.1016/j.omto.2021.03.006
122. Sekar T V., Foygel K, Willmann JK, Paulmurugan R. Dual-therapeutic reporter genes fusion for enhanced cancer gene therapy and imaging. *Gene Ther*. 2013;20(5):529-537. doi:10.1038/gt.2012.66
123. Liu X, Huang H, Gao Y, et al. Visualization of gene therapy with a liver cancer-targeted adeno-associated virus 3 vector. *J Cancer*. 2020;11(8):2192-2200. doi:10.7150/jca.39579
124. Alan R. Penheiter, Stephen J. Russell, Stephanie K. Carlson. The Sodium Iodide Symporter (NIS) as an Imaging Reporter for Gene, Viral, and Cell-based Therapies. *Curr Gene Ther*. 2012;12(1):33-47. doi:10.2174/156652312799789235
125. Ravera S, Reyna-Neyra A, Ferrandino G, Amzel LM, Carrasco N. The Sodium/Iodide Symporter (NIS): Molecular Physiology and Preclinical and Clinical Applications. *Annu Rev Physiol*. 2017;79:261-289. doi:doi:10.1146/annurev-physiol-022516-034125.
126. Moulay G, Ohtani T, Ogut O, et al. Cardiac AAV9 gene delivery strategies in adult canines: Assessment by long-term serial SPECT imaging of sodium iodide symporter expression. *Mol Ther*. 2015;23(7):1211-1221. doi:10.1038/mt.2015.78
127. Lehner S, Lang C, Kaissis G, et al. 124I-PET Assessment of Human Sodium Iodide Symporter Reporter Gene Activity for Highly Sensitive In Vivo Monitoring of Teratoma

Formation in Mice. *Mol Imaging Biol*. 2015;17(6):874-883. doi:10.1007/s11307-015-0857-1
128. Müller AM, Schmohl KA, Knoop K, et al. Hypoxia-targeted 131 I therapy of hepatocellular cancer after systemic mesenchymal stem cell-mediated sodium iodide symporter gene delivery. *Oncotarget*. 2016;7(34). www.impactjournals.com/oncotarget/.
129. Shi S, Zhang M, Guo R, Miao Y, Li B. Bone Marrow-Derived Mesenchymal Stem Cell-Mediated Dual-Gene Therapy for Glioblastoma. *Hum Gene Ther*. 2019;30(1):106-117. doi:10.1089/hum.2018.092
130. Tutter M, Schug C, Schmohl KA, et al. Effective control of tumor growth through spatial and temporal control of theranostic sodium iodide symporter (NIS) gene expression using a heat-inducible gene promoter in engineered mesenchymal stem cells. *Theranostics*. 2020;10(10):4490-4506. doi:10.7150/thno.41489
131. Gray-Edwards HL, Regier DS, Shirley JL, et al. Novel Biomarkers of Human GM1 Gangliosidosis Reflect the Clinical Efficacy of Gene Therapy in a Feline Model. *Mol Ther*. 2017;25(4):892-903. doi:10.1016/j.ymthe.2017.01.009
132. Ahmed SS, Li H, Cao C, et al. A single intravenous rAAV injection as late as P20 achieves efficacious and sustained CNS gene therapy in Canavan mice. *Mol Ther*. 2013;21(12):2136-2147. doi:10.1038/mt.2013.138
133. Taghian T, Batista AR, Kamper S, et al. Real-time MR tracking of AAV gene therapy with βgal-responsive MR probe in a murine model of GM1-gangliosidosis. *Mol Ther - Methods Clin Dev*. 2021;23(December):128-134. doi:10.1016/j.omtm.2021.08.003
134. Ren J, Chen YI, Liu CH, Chen P, Prentice H, Liu PK. Noninvasive Tracking of Gene Transcript and Neuroprotection after Gene Therapy. *Gene Ther*. 2016;23(1):1-9. doi:10.1038/gt.2015.81.
135. Christine CW, Bankiewicz KS, Van Laar AD, et al. Magnetic resonance imaging–guided phase 1 trial of putaminal AADC gene therapy for Parkinson's disease. *Ann Neurol*. 2019;85(5):704-714. doi:10.1002/ana.25450
136. Minn I, Bar-Shir A, Yarlagadda K, et al. Tumor-Specific Expression and Detection of a CEST Reporter Gene. *Magn Reson Med*. 2015;74(2):544-549. doi:10.1002/mrm.25748.Tumor-Specific
137. Robinson TM, Ho ML, Wahlig B, et al. An essential N-terminal serine-rich motif in the AAV VP1 and VP2 subunits that may play a role in viral transcription. *Virology*. 2020;546(April):127-132. doi:10.1016/j.virol.2020.04.008
138. Chen MY, Chen W, Tong J, Ho ML, Suh J. N-terminal serine/threonine motif has diverse and important effects on behavior of multiple AAV serotypes. *Virology*. 2021;563(April):107-115. doi:10.1016/j.virol.2021.08.010
139. Gabriel N, Hareendran S, Sen D, et al. Bioengineering of AAV2 capsid at specific serine, threonine, or lysine residues improves its transduction efficiency in vitro and in vivo. *Hum Gene Ther Methods*. 2013;24(2):80-93. doi:10.1089/hgtb.2012.194
140. Zaiss M, Schmitt B, Bachert P. Quantitative separation of CEST effect from magnetization transfer and spillover effects by Lorentzian-line-fit analysis of z-spectra. *J Magn Reson*. 2011;211(2):149-155. doi:10.1016/j.jmr.2011.05.001
141. Chan KWY, Jiang L, Cheng M, et al. CEST-MRI detects metabolite levels altered by breast cancer cell aggressiveness and chemotherapy response. *NMR Biomed*. 2016;29(6):806-816. doi:10.1002/nbm.3526.CEST-MRI
142. Zhang XY, Zhai Y, Jin Z, Li C, Sun PZ, Wu Y. Preliminary demonstration of in vivo

quasi-steady-state CEST postprocessing—Correction of saturation time and relaxation delay for robust quantification of tumor MT and APT effects. *Magn Reson Med*. 2021;86(2):943-953. doi:10.1002/mrm.28764
143. Xu X, Xu J, Chan KWY, et al. GlucoCEST Imaging with On-Resonance Variable Delay Multiple Pulse (onVDMP) MRI. *Magn Reson Med*. 2019;81(1):47-56. doi:10.1002/mrm.27364.GlucoCEST
144. Ho TC, Chang CC, Chan HP, et al. Hydrogels: Properties and Applications in Biomedicine. *Molecules*. 2022;27(9):1-29. doi:10.3390/molecules27092902
145. Correa S, Grosskopf AK, Lopez Hernandez H, et al. Translational Applications of Hydrogels. *Chem Rev*. 2021;121(18):11385-11457. doi:10.1021/acs.chemrev.0c01177
146. Zhao Y, Zhang J, Wang X, et al. The osteogenic effect of bone morphogenetic protein-2 on the collagen scaffold conjugated with antibodies. *J Control Release*. 2010;141(1):30-37. doi:10.1016/j.jconrel.2009.06.032
147. Chen Q, Wang C, Zhang X, et al. In situ sprayed bioresponsive immunotherapeutic gel for post-surgical cancer treatment. *Nat Nanotechnol*. 2019;14(1):89-97. doi:10.1038/s41565-018-0319-4
148. Zhao N, Suzuki A, Zhang X, et al. Dual Aptamer-functionalized In Situ Injectable Fibrin Hydrogel for Promotion of Angiogenesis via Co-delivery of VEGF and PDGF-BB. *ACS Appl Mater Interfaces*. 2019;11(20):18123-18132. doi:10.1159/000444169.Carotid
149. Kim IL, Khetan S, Baker BM, Chen CS, Jason A. Fibrous hyaluronic acid hydrogels that direct MSC chondrogenesis through mechanical and adhesive cues. *Biomaterials*. 2013;34(22):5571-5580. doi:10.1016/j.biomaterials.2013.04.004.Fibrous
150. Xu K, Lee F, Gao SJ, Chung JE, Yano H, Kurisawa M. Injectable hyaluronic acid-tyramine hydrogels incorporating interferon-α2a for liver cancer therapy. *J Control Release*. 2013;166(3):203-210. doi:10.1016/j.jconrel.2013.01.008
151. Lueckgen A, Garske DS, Ellinghaus A, Mooney DJ, Duda GN, Cipitria A. Enzymatically-degradable alginate hydrogels promote cell spreading and in vivo tissue infiltration. *Biomaterials*. 2019;217(May):119294. doi:10.1016/j.biomaterials.2019.119294
152. Jeon O, Powerll C, Solorio LD, Krebs MD, Alsberg E. Affinity-based growth factor delivery using biodegradable, photocrosslinked heparin-alginate hydrogels. *J Control Release*. 2011;154(3):258-266. doi:10.1016/j.jconrel.2011.06.027.Affinity-based
153. Ma H, He C, Cheng Y, et al. PLK1shRNA and doxorubicin co-loaded thermosensitive PLGA-PEG-PLGA hydrogels for osteosarcoma treatment. *Biomaterials*. 2014;35(30):8723-8734. doi:10.1016/j.biomaterials.2014.06.045
154. Li D, Zhou J, Zhang M, et al. Long-term delivery of alendronate through an injectable tetra-PEG hydrogel to promote osteoporosis therapy. *Biomater Sci*. 2020;8(11):3138-3146. doi:10.1039/d0bm00376j
155. Liu J, Zhang SM, Chen PP, et al. Controlled release of insulin from PLGA nanoparticles embedded within PVA hydrogels. *J Mater Sci Mater Med*. 2007;18(11):2205-2210. doi:10.1007/s10856-007-3010-0
156. Norouzi M, Nazari B, Miller DW. Injectable hydrogel-based drug delivery systems for local cancer therapy. *Drug Discov Today*. 2016;21(11):1835-1849. doi:10.1016/j.drudis.2016.07.006
157. Zou T, Jiang S, Yi B, Chen Q, Heng BC, Zhang C. Gelatin methacrylate hydrogel loaded with brain-derived neurotrophic factor enhances small molecule-induced neurogenic differentiation of stem cells from apical papilla. *J Biomed Mater Res - Part A*.

2022;110(3):623-634. doi:10.1002/jbm.a.37315
158. Li J, Zhang Y, Zhu L, Chen K, Li X, Xu W. Smart Nucleic Acid Hydrogels with High Stimuli-Responsiveness in Biomedical Fields. *Int J Mol Sci*. 2022;23(3). doi:10.3390/ijms23031068
159. Liu AL, Garcia AJ. Methods for Generating Hydrogel Particles for Protein Delivery. *Annu Rev Biomed Eng*. 2016;44(6):1946-1958. doi:10.1007/s10439-016-1637-z.Methods
160. Bae KH, Kurisawa M. Emerging hydrogel designs for controlled protein delivery. *Biomater Sci*. 2016;4(8):1184-1192. doi:10.1039/c6bm00330c
161. Huang Z, Delparastan P, Burch P, Cheng J, Cao Y, Messersmith PB. Injectable dynamic covalent hydrogels of boronic acid polymers cross-linked by bioactive plant-derived polyphenols. *Biomater Sci*. 2018;6(9):2487-2495. doi:10.1039/C8BM00453F
162. Yesilyurt V, Webber MJ, Appel EA, Godwin C, Langer R, Anderson DG. Injectable Self-Healing Glucose-Responsive Hydrogels with pH-Regulated Mechanical Properties. *Adv Mater*. 2016;28(1):86-91. doi:10.1002/adma.201502902
163. Marco-Dufort B, Willi J, Vielba-Gomez F, Gatti F, Tibbitt MW. Environment Controls Biomolecule Release from Dynamic Covalent Hydrogels. *Biomacromolecules*. 2021;22(1):146-157. doi:10.1021/acs.biomac.0c00895
164. Narayanaswamy R, Torchilin VP. Hydrogels and their applications in targeted drug delivery. *Molecules*. 2019;24(3). doi:10.3390/molecules24030603
165. Wang Y, Bruggeman KF, Franks S, et al. Is Viral Vector Gene Delivery More Effective Using Biomaterials? *Adv Healthc Mater*. 2021;10(1):1-25. doi:10.1002/adhm.202001238
166. Miyahara H, Kurashina Y, Ogawa Y, et al. Hierarchical Hydrogel Drug Delivery System Enables Controlled Release of Adeno-Associated Viruses for Gene Therapy. *Proc IEEE Int Conf Micro Electro Mech Syst*. 2019;2019-Janua(January):601-602. doi:10.1109/MEMSYS.2019.8870781
167. Remes A, Basha DI, Puehler T, et al. Alginate hydrogel polymers enable efficient delivery of a vascular-targeted AAV vector into aortic tissue. *Mol Ther - Methods Clin Dev*. 2021;21(June):83-93. doi:10.1016/j.omtm.2021.02.017
168. Kishnani PS, Sun B, Koeberl DD. Gene therapy for glycogen storage diseases. *Hum Mol Genet*. 2019;28(R1):R31-R41. doi:10.1093/hmg/ddz133
169. Piepho AB, Lowe J, Cumby LR, et al. Micro-dystrophin gene therapy demonstrates long-term cardiac efficacy in a severe Duchenne muscular dystrophy model. *Mol Ther Methods Clin Dev*. 2023;28(March):344-354. doi:10.1016/j.omtm.2023.02.001
170. Wang S, Li Y, Xu Y, et al. AAV Gene Therapy Prevents and Reverses Heart Failure in A Murine Knockout Model of Barth Syndrome. *Circ Res*. 2020;126(8):1024-1039. doi:10.1161/CIRCRESAHA.119.315956.AAV
171. Ribieras AJ, Ortiz YY, Li Y, et al. E-Selectin/AAV Gene Therapy Promotes Myogenesis and Skeletal Muscle Recovery in a Mouse Hindlimb Ischemia Model. *Cardiovasc Ther*. 2023;2023. doi:10.1155/2023/6679390
172. Chen L, Xu X, Zeng H, et al. Separating Fast and Slow Exchange Transfer and Magnetization Transfer Using Off-resonance Variable Delay Multiple Pulse (VDMP) MRI. *Magn Reson Med*. 2018;80(4):1568-1576.
173. Lin EC, Li H, Zu Z, et al. Chemical exchange rotation transfer (CERT) on human brain at 3 T. *Magn Reson Med*. 2018;80(6):2609-2617.
174. Wu L, Lu D, Sun PZ. Comparison of model-free Lorentzian and spinlock model-based fittings in quantitative CEST imaging of acute stroke. *Magn Reson Med*. 2023;90(5):1958-

1968. doi:10.1002/mrm.29772
175. Sun PZ. Quasi-steady-state chemical exchange saturation transfer (QUASS CEST) solution improves the accuracy of CEST quantification - QUASS CEST MRI-based omega plot analysis. *Magn Reson Med*. 2021;86(2):139-148. doi:10.1159/000444169.Carotid